CDF/DOC/PLUG_UPGR/CDFR/4659
Version 2

Proposal of the Plug Preshower Detector (II)

— Readout System —

M. Albrow[b], G. Apollinari[f], T. Asakawa[g], P. de Barbaro[e], V. Barnes[d], R. Harris[b], J. Huston[c], S.H. Kim[g], M. Lindgren[a], T. Nakayama[g], R. Oishi[g], Y. Seiya[g], M. Shimojima[g]

(a) University of California at Los Angeles, (b) Fermilab, (c) Michigan State University, (d) Purdue University, (e) University of Rochester, (f) Rockefeller University, (g) University of Tsukuba

Abstract

In the present baseline scheme, the first layer of the CDF plug upgrade electromagnetic calorimeter supposed to act as a preshower detector is not provided with any dedicated readout systems nor is included in the tower readout of the calorimeter, but is just floating. We propose to install a readout system of the plug preshower detector, which consists of electrical cables and readout electronics. The main purposes of the preshower detector are to extract a prompt photon fraction and to improve the electron identification. The plug region is important in the photon physics because of its sensitivity to the gluon PDF in lower x and other physics observables in kinematically extended regions compared with the central. Also, acceptance of photons and electrons are increased. We expect a 30% gain of top events in the $t \to W \to e$ channel by including plug electrons. The $W(\to e\nu)\gamma$ acceptance increases by a factor of 3 including plug photons and electrons. The preshower detector is indispensable for any precision measurements involving the prompt photons. Test beam data taken in 1997 show that the plug preshower detector has a good efficiency for detecting photon conversions with an acceptable noise occupancy. The electron identification in the plug region will be significantly improved from Run I, for the most part, by an extended implementation of a tracking system and by the upgraded calorimeter. The signal-to-background ratio in the plug region is, however, lower than the central. Depending on the physics process, the ratios normalized to those in the central region are $0.3 \sim 0.8$. From the test beam data, an additional reduction factor for the charged hadron background by a use of the preshower detector is obtained to be $\simeq 2$. The plug preshower detector is, therefore, necessary to improve the electron quality in the plug region to a level similar to the central electrons. Total cost for installation of the electrical cables and readout electronics is estimated to be $\simeq$ \$88k. There is no concern about delays in the overall schedule of the CDF upgrade due to the installation of the preshower detector because it can be merged into the on-going activities for the baseline detector in a quite straightforward way. Immediate importance right now will be the electrical cables. At least they must be in place prior to the detector roll-in to avoid any cabling works which are obviously very inefficient in the collision hall.

1 Plug Preshower Detector

The CDF Plug Upgraded Electromagnetic Calorimeter (PEM) is described in detail elsewhere [1]. The PEM detector consists of 23 sampling layers of tile-fiber system and covers a pseudorapidity range of $1.1 < |\eta| < 3.6$. The readout systems (960 channels in total) of the first PEM layer could be separated from the rest of the layers and used as a preshower detector. We use HAMAMATSU R5900 (multianode PMT with 16 channels) as the photon readout. The amount of material in front of the PEM is 2 X_0 including a preradiator (the front cover plate of the PEM), the COT end-plate, SVX-II, ISL, and beam-pipe. We have already proposed to install the Plug Preshower (PPR) tile-fibers and preradiator material and had it approved [2]. In this note, we propose to install the readout systems for the PPR, which consists of signal cables, HV cables and readout electronics. The photon and electron identification in the plug region will be significantly improved compared with the situation in Run I mainly because of the tracking upgrade in this region, and of the improved calorimetry. The PPR is a critical detector for the statistical separation between photons and neutral hadrons (γ-π^0 separation). It also provides another handle to control charged hadron background in the electron identification (e-π separation). Another purpose is to improve the linearity of the PEM for low energies by adding the PPR response to the EM with optimized weight factors.

2 Tracking System

In Run I and before, we suffered from the poor tracking information in the plug region, as shown in Figure 1, for the photon and electron identification. In Run II, an efficient tracking system consisting of the SVX II, ISL and a part of the COT will be available in the plug region ($1 < |\eta| < 2$). We summarize the tracking coverage and expected momentum resolution in Table 1 [1]. Given the tracking and calorimeter performance in the plug region similar to the central region, we will have an opportunity to extend the effective identification of photons and electrons into a high η region from Run II.

3 Photon Identification

For the photon detection, the main background is an isolated $\pi^0 \to \gamma\gamma$ observed as a single EM cluster. The Central Preshower detector (CPR) installed in $|\eta| < 0.9$ successfully enabled the background subtraction and could reduce the systematic uncertainty on the background subtraction. The γ-π^0 separation using the preshower detector has advantages of the energy independence and the capability in higher energy regions ($E_T > 40$ GeV) unlike the shower profile method using a shower maximum detector. The fraction of photons (f_γ) in a sample can be estimated by

$$f_\gamma = \frac{P_o - P_{\pi^0}}{P_\gamma - P_{\pi^0}}, \quad (1)$$

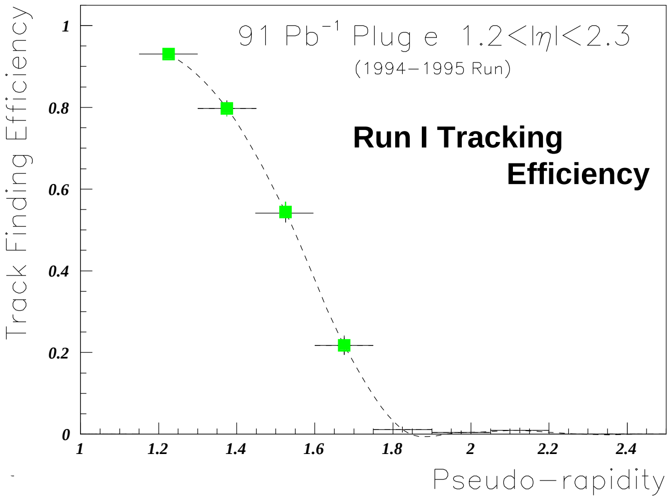

Figure 1: Track finding efficiency measured by using electrons in Run I.

	Tracking Coverage
SVX II	$\|\eta\| \leq 2$
ISL (1 layer)	$\|\eta\| \leq 1$
(2 layers)	$1 \leq \|\eta\| \leq 2$

	Momentum Resolution
	$\Delta p_T/p_T^2$
COT	0.3%
SVX II+ISL	0.4%
SVX II+ISL+COT	0.08%

Table 1: Tracking coverage and momentum resolution.

where P_γ and P_{π^0} are the non-conversion probabilities for a true photon and π^0 background respectively, and P_o is the observed fraction of the EM showers which do not convert in the preshower detector.

3.1 Statistical Uncertainty

For a given number of neutral EM showers, the statistical uncertainty of the photon fraction depends on the amount of the material present before the detector via the denominator $P_\gamma - P_{\pi^0}$ in (1), and the photon fraction itself. We show the non-conversion probabilities for γ and π^0, and their difference as a function of the preradiator thickness in Figure 2. The difference is maximum at 0.9 X_0. The optimum material amount is, in fact, changes along the photon fraction as seen in Figure 3 where the statistical uncertainty on the estimated number of photons is shown for the case of 100 true photons. For the

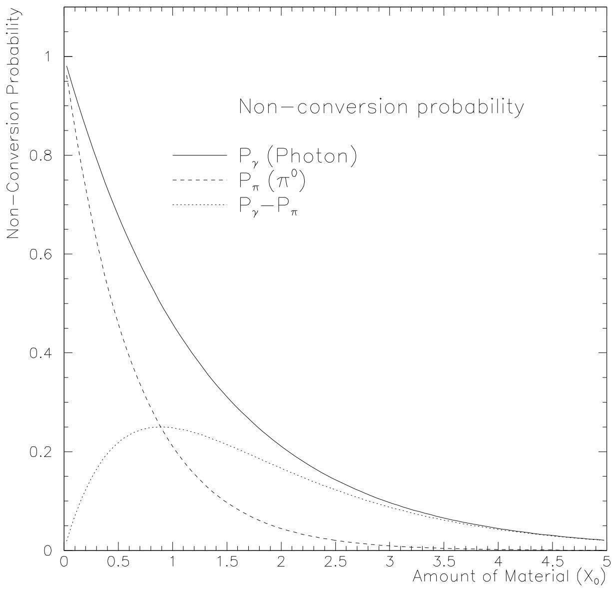

Figure 2: Non-conversion probabilities for single photon (solid) and $\pi^0 \to \gamma\gamma$ (dashed), and their difference (dotted) of $P_\gamma - P_{\pi^0}$.

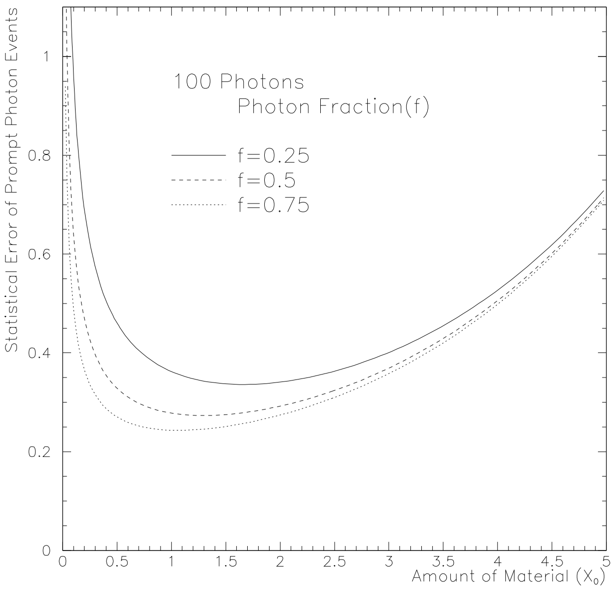

Figure 3: Statistical uncertainty as a function of the material thickness for photon fractions ($f = 0.25$, 0.5 and 0.75) in the case of 100 true photons.

50% photon fraction, for example, the preradiator thickness of $0.7 \sim 2.1\ X_0$ is acceptable for which the statistical uncertainty is stable within 30%. Note the optimal choice of the thickness is different for the e-π separation. The pion rejection is more powerful for thicker material. A preradiator thickness of $1.5 \sim 2.0\ X_0$ is a reasonable compromise to perform both of the γ-π^0 and e-π separation, that is described in Ref. [2].

The photo fraction is determined by the relative rate of the prompt photons to the backgrounds. An isolation cut can significantly reduce the background. A comparison of the background rates in the central and plug region is given in Figure 4 which shows the rapidity distribution for isolated and non-isolated π^0/η's. The background rate is almost the same as the central with little dependence on the isolation requirement, therefore only the signal rate is the issue. Figure 5 shows the measured photon fraction in the plug region using Run 0 data ($E_T^\gamma > 23$ GeV) as a function of the isolation cut ($\sum E_T$ in $R < 0.7$) which is the extra energy sum around the photon. Using a tight isolation cut of $\sum E_T < 3$ GeV, the photon fraction in the observed EM clusters is increased to 0.49 ± 0.09 [3].

From Figure 3 with taking $2\ X_0$ and the 50% photon fraction, the statistical uncertainty of the photon fraction expected for the plug region is given by $\Delta N_\gamma / N_\gamma \simeq 300\%/\sqrt{N_\gamma}$.

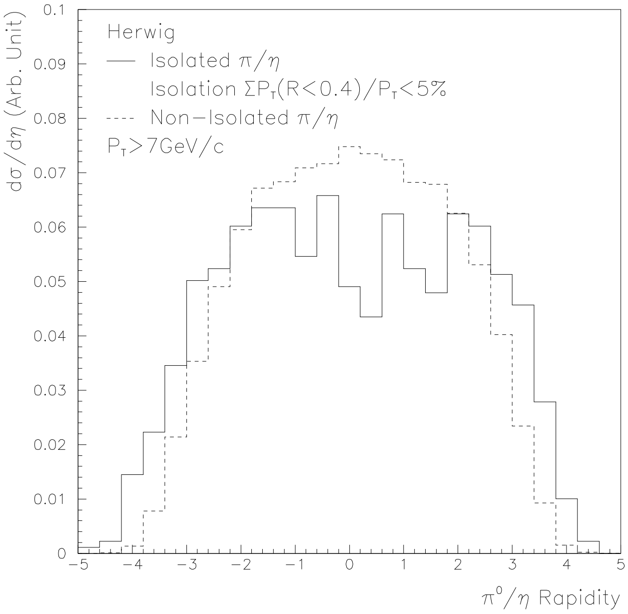

Figure 4: Rapidity distribution for isolated (solid) and non-isolated (dashed) π^0/η's with p_T >7 GeV/c. A cone isolation ($R < 0.4$) of $\sum p_T/p_T$ is required to be smaller than 5%.

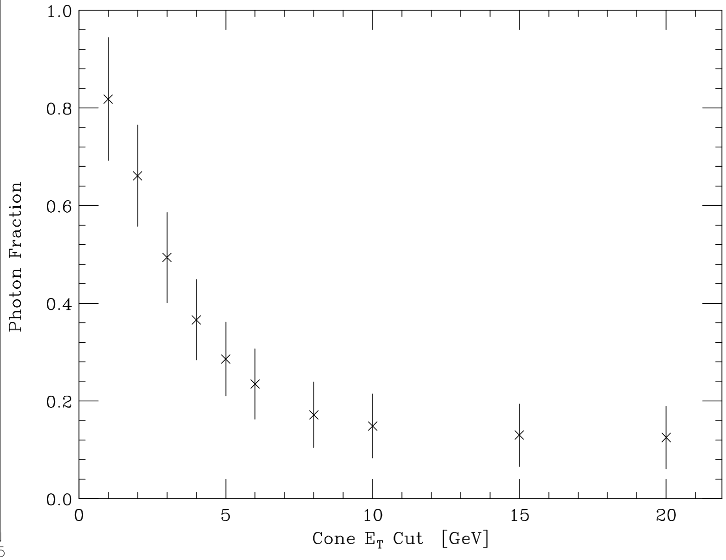

Figure 5: Photon fraction in the Run 0 plug photon candidates ($E_T^\gamma > 23$ GeV) as a function of the isolation cut, where the isolation is an extra sum E_T in $R < 0.7$ around the photon.

3.2 Systematic Uncertainty

Systematic uncertainty of the photon fraction arises from uncertainties of the non-conversion probabilities, P_γ and P_{π^0}. There are a few sources of the uncertainties.

3.2.1 Multiphoton

Multiphotons such as $\eta \to \pi^0\pi^0\pi^0$ observed as a single EM cluster is another background source for the prompt photons. The non-conversion probabilities for these backgrounds are different from that for a single π^0. CDF measured the production ratio of η and π^0 and estimated the fraction of the backgrounds using the measured ratio and the simulation. The fraction of $\eta \to \pi^0\pi^0\pi^0$ in the neutral meson decay background is 20% including the efficiency and branching ratio [4]. Figure 6 shows the change of the systematic uncertainty as a function of the fraction of such backgrounds as $\omega \to \pi^0\gamma$, $K^0 \to \pi^0\pi^0$ and $\eta \to \pi^0\pi^0\pi^0$ in the neutral meson decay background. The systematic uncertainty is expected to be $\simeq 5\%$ unless we do not evaluate the contribution from these backgrounds to a sample and do not apply a correction to the non-conversion probability.

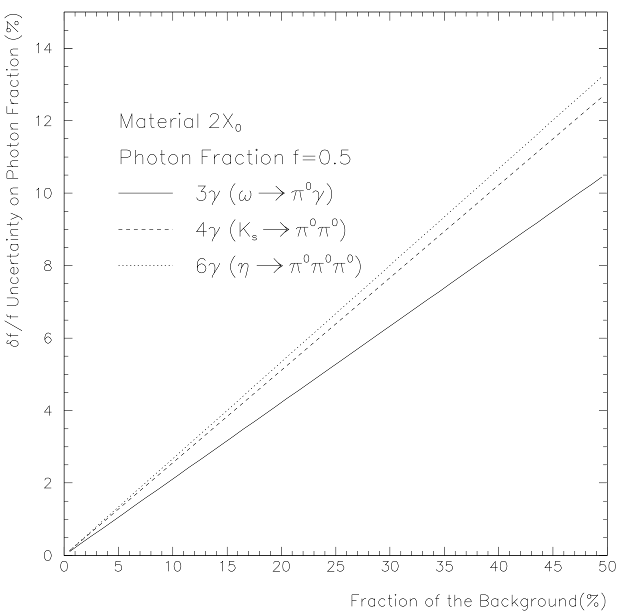

Figure 6: Systematic uncertainty on the photon fraction as a function of the fraction of other backgrounds (3, 4 and 6 γ's) in all the neutral meson decay background. The photon fraction of 50% is used in this plot.

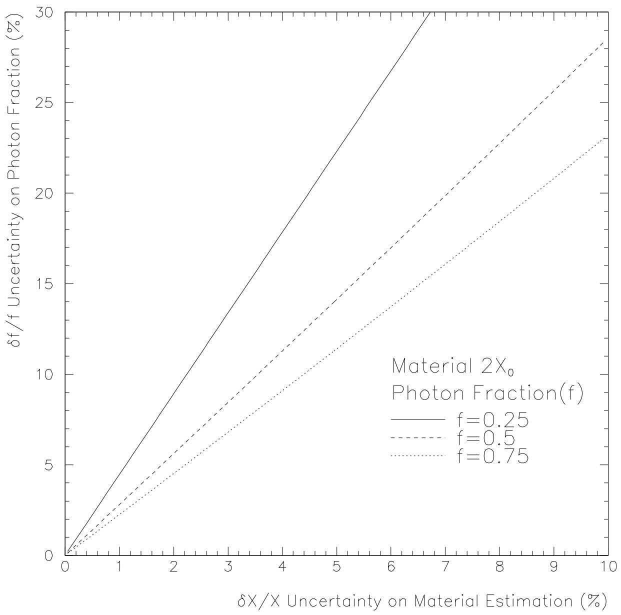

Figure 7: Systematic uncertainty on the photon fraction as a function of the uncertainty of material estimation.

3.2.2 Estimation of the Material Amount

The largest systematic uncertainty comes from the uncertainty in estimating the amount of the material, which will be used to determine the non-conversion probabilities. In Run I, we measured the amount of the material in front of the CPR within 3.8% using $\rho^+ \to \pi^0\pi^+$ and $\pi^0/\eta \to \gamma\gamma$ samples [5]. Using the informations of the shower max and the tracking detectors, we can reconstruct the $\pi^0/\eta \to \gamma\gamma$ and $\rho^+ \to \pi^0\pi^+$ which are the same technique in the central photon analysis [6]. Figure 7 shows the systematic uncertainty on the photon fraction coming from the material estimation. This shows a 4% change in the material estimation corresponds to an 11% change in the photon fraction for the photon fraction $\simeq 0.5$. The improvement in Run II depends on the sample size of these control samples collected with a special trigger.

3.2.3 Inefficiency of the Photon Conversion Detection and Noise

Readout device of the preshower is required to have a high efficiency for detecting the photon conversions with a low noise occupancy. Presence of the inefficiency and the noise occupancy results in the observed non-conversion probabilities different from the true values. In a test beam analysis, as discussed later in Section 6.1, the PPR efficiency was

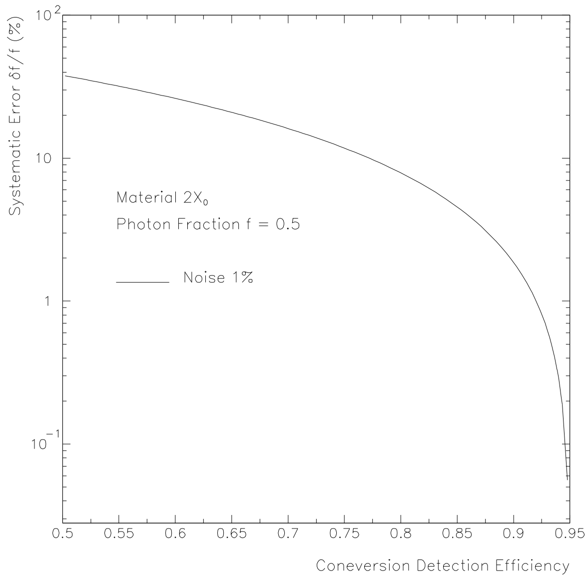

Figure 8: Systematic uncertainty of the photon fraction as a function of the photon detection efficiency for the case of 1% noise occupancy.

Source	Uncertainty
≥ 3 photons	5%
Material	5%
Inefficiency and noise	2%
Backscattered shower	3%
Total	8%

Table 2: A rough estimation of the systematic uncertainty of the photon fraction.

measured to be $\simeq$ 90% with the noise occupancy smaller than 1% corresponding to a photon-fraction uncertainty of $\simeq$ 2% as seen from Figure 8.

3.2.4 Backscattered Shower

Fragments of the EM showers scattered backward at layers behind the preshower counter mimic the photon conversion signals. By using a shower simulation, the effect from this source on the photon fraction was estimated to be $\simeq$ 2% at $p_T = 16$ GeV/c and $\simeq$ 7% at $p_T = 100$ GeV/c [7]. As in the case of the multiphotons, they have to be included in the systematic uncertainty if we do not correct for it.

3.3 Summary of the Uncertainty in the Photon Measurement

We summarized the uncertainties in estimation of the prompt photon fraction in Table 2. The systematic uncertainties due to the multiphotons and the backscattered shower are included conservatively assuming no explicit correction is made. The numbers of the systematic uncertainties from the material estimation has been chosen somewhat arbitrarily assuming the size of the control sample 4 times as large as the one in Run I. The total uncertainty in the number of prompt photons is, then, given by

$$\frac{\Delta N_\gamma}{N_\gamma} \simeq \frac{300\%}{\sqrt{N_\gamma}} \oplus 8\%.$$

As shown later, the total uncertainty less than 5% will be necessary to constraint the different gluon PDF's. It is expected that a certain level of efforts in reducing the systematic uncertainty will be required in Run II where the statistical uncertainty is typically $\simeq 1\%$.

4 Electron Identification

By the extension of the tracking system and the upgrade calorimeter in the plug region, both with performances similar to the central, it should be a reasonable statement that we have tools with uniform performances for the electron identification in all the η regions up to $\eta = 2$ in Run II.

The PPR will be also used in the electron identification for the event-by-event rejection of charged hadron faking the electron[1]. In Run I, by requiring a large CPR pulse height corresponding to 4 minimum ionizing particles (MIP's), we could reduce the backgrounds of charged hadrons in the soft electron tagging. A use of the CPR was not in the *standard* electron selection in high energy regions. It tends to be used in the low-energy electron identification where the signal-to-background ratio (S/N) is more severe. The PPR performance for the background reduction is found to be similar to the CPR from the PPR test beam results, which will be discussed in Section 6.2.

In discussing the benefits of the PPR to the electron sample quality, we focus on the S/N in the plug region relative to the central. Assuming that the efficiency of the electron identification in the plug region is similar to the central, we avoid detailed detector simulations to estimate the relative S/N in a sample. We first check the background rate in the plug region compared with the central. Figure 9 shows the η distributions for isolated charged hadrons for the transverse momentum p_T >2, 12 and 25 GeV/c, which are obtained by the HERWIG generator. The isolation ($I = \sum p_T/p_T$) of charged hadrons was required as $I < 0.1$, where the p_T is the transverse momentum of the charged hadron, $\sum p_T$ is for charged and neutral particles in $R < 0.4$ around the charged hadron. The distributions are almost flat. The S/N depends on physics processes which will be discussed in each subsection of physics motivations. Generally, the S/N in the plug region is worse than the central even for high energy regions. As a possible scenario, we will have to use the PPR in a standard plug-electron selection in Run II.

[1]It can be used for the statistical separation to estimate the background fraction in an electron sample. We primarily consider the hadron rejection as the PPR use in this note.

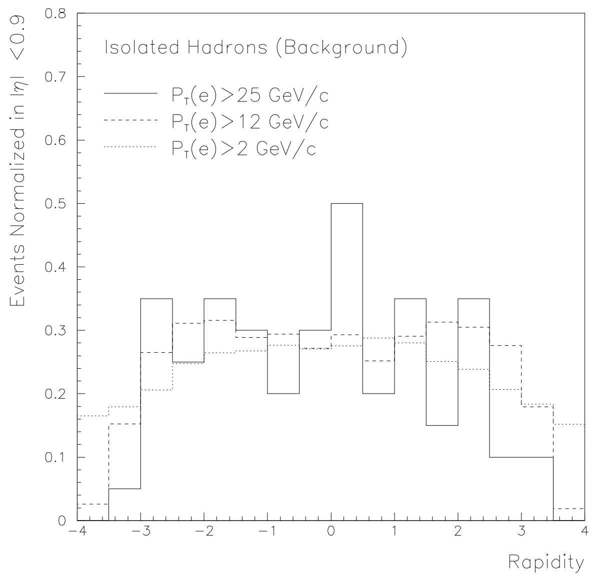

Figure 9: Pseudorapidity distributions for isolated charged hadrons (HERWIG) for $p_T >$ 2, 12 and 25 GeV/c.

5 Physics Motivations

The PPR is used to determine the fraction of prompt photons as well as to eliminate the charged hadron backgrounds enabling us to use photons and electrons in the high η region ($1 < |\eta| < 2$). It gives us many topics in the physics of top quark, electroweak, QCD, bottom quark and in new physics searches[2].

5.1 Triggers

We summarized the proposed Run II triggers relevant to the plug electrons and photons in Table 3 collected from the trigger working group Web page. We will discuss the physics gains using the plug electrons and photons possible in a range covered by these triggers. Basically, it is possible to do the QCD photon, Top and W physics using the triggered electrons and photons in the plug region. In the b physics, however, we may have to start from samples collected by the central triggers, which means that we are limited mostly to the dilepton sample. There are also enough opportunities for the plug electrons and photons to contribute to new physics searches. Since the PPR itself is used for the statistical separation in photon analyses, new physics searches using photons are not relevant in the context of the PPR installation.

[2]We did not have time to include discussions on the new physics searches in this note.

Triggers	Comments
"Photon"	
EM $E_T > 23$ GeV, Isolated	single photon: QCD
Two EM $E_T > 16$ GeV	diphoton: QCD
	dielectron: Top, Z, New Physics
"Electron"	
EM $E_T > 18$ GeV + $\not\!\!E_T$	W, Top, New Physics
Two EM $E_T > 18$ GeV	diphoton: QCD
	dielectron: Top, Z, New Physics
EM $E_T > 50$ GeV	plug electron inclusive
CEM-Track $E_T > 18$ GeV	central electron (CEM) inclusive
	CEM-PEM dielectron: Top, Bottom, New Physics
"Muon"	
CMUP $p_T > 18$ GeV/c	central muon (CMU) inclusive
	CMU-PEM: Top, Bottom, New Physics

Table 3: Proposed Run II triggers relevant to plug electrons and photons.

5.2 QCD Physics

5.2.1 Prompt Photon

The direct photon production is one of precision QCD tests, because there is an advantage of precision measurement of photon energy rather than jets. The inclusive photon cross section was successfully measured using Run IA data (see Figure 10), where the photons were identified with the CPR and strip chamber [7]. The measured cross section agrees with a NLO prediction within a wide photon transverse energy range up to 120 GeV. So far, only the integrated cross section of the plug photons within $1.2 < |\eta| < 2.2$ has been measured to be $1451 \pm 85(\text{stat}) \pm 259(\text{syst})$ pb using Run 0 data with larger systematics than that of the central analysis. Figure 11 shows the integrated cross section of prompt photons in the central and plug regions. In Run II (2 fb^{-1}), including photons in the plug region using the PPR, the measurement can be extended to over E_T=200 GeV within 5% statistical uncertainty in 175< E_T <225 GeV (the contribution of plug photons is 20%), where the inclusive jet cross section has a discrepancy of 10% level between the experiment and theories. The estimated statistical uncertainty takes into account of the 40% efficiency of the photon identification after geometrical acceptance and E_T cut obtained for the central photon in the Run I analysis. We assumed the same efficiency for the plug photons here and in what follows.

The angular distribution in the CM system of γ+jet events is another example of the precision QCD tests on the production mechanism [8]. Figure 12 shows the measured photon angular distribution in Run I. There is a 30% discrepancy from a NLO calculation already at $\cos\theta^* \simeq 0.75$. The Run II data including the plug photons will cover the region

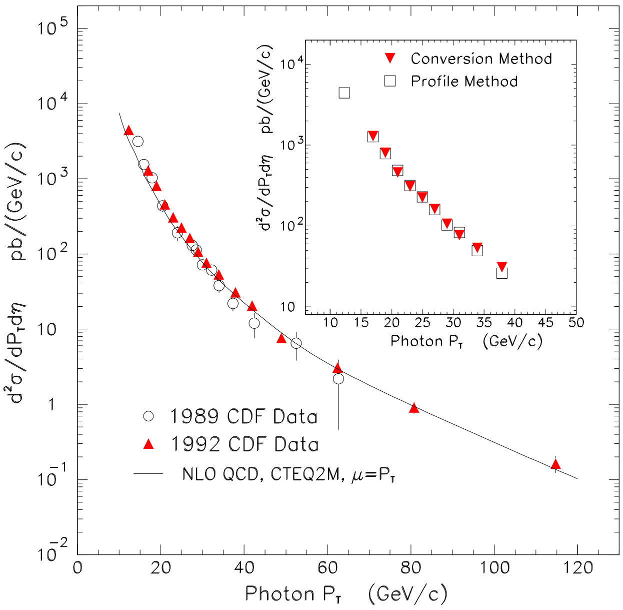

Figure 10: Inclusive prompt photon cross sections from Run 0 (in 1989) and Run IA (in 1992) compared with a NLO QCD prediction. Inset is the comparison of the two background subtraction methods.

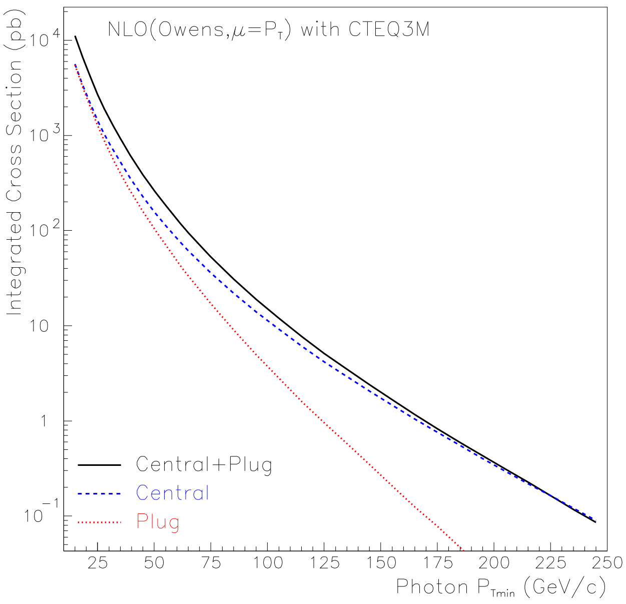

Figure 11: Integrated cross sections of prompt photons in the central (dashes), plug (dots) and central+plug (solid) regions.

$|\cos\theta^*| < 0.96$. In the Run I analysis, η regions of the photon and jet were chosen so that the $\cos\theta^*$ is free from biases due to the geometrical acceptance, in order to avoid correction for it. An example of such regions for $\cos\theta^* > 0.8$ including the plug region is given in Figure 13. Expected Run-II statistics in the box corresponding to the plug region in the figure is $\simeq$ 109k events giving a $\simeq 1\%$ statistical uncertainty. It is 1.5 times as large as the central statistics.

The photon production is also a way to study the gluon distribution function in the proton because $\simeq 80\%$ of the production proceeds via the Compton process at the Tevatron energy. In general, the plug region is more sensitive to lower and higher x regions of the PDF's compared with the central as seen in Figures 14 $\sim$ 17, where the gluon and the valence u-quark PDF's, relevant to the γ+jet events, are shown in ranges accessed by the lower and higher-x initial partons, respectively. Recently, CDF has published a measurement of the jet rapidity in the central photon events [9], however, the statistics was limited and the analysis was geometrically restricted. Figure 18 shows the jet rapidity distributions in prompt photon events (Owens NLO) with various PDF's. The plug photon+plug jet events ($1 \leq |\eta_\gamma| \leq 2$, $2 \leq |\eta_{\rm jet}| \leq 3$) are more sensitive to the PDF's compared with the central. We expect 260k plug photon events in Run II, which corresponds to $< 1\%$ statistical uncertainty. The plug region is statistically 2 times as powerful as the

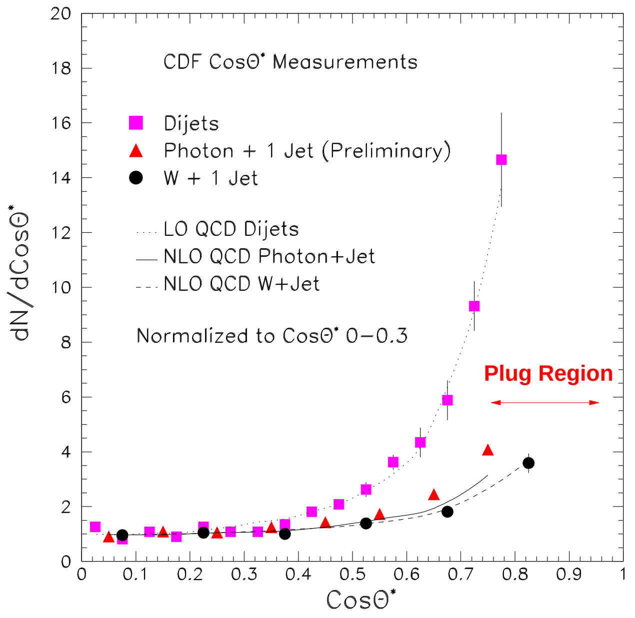

Figure 12: Prompt photon, dijet and W+jet $dN/d(\cos\theta^*)$ after background subtraction. The photon data (triangle) are compared to NLO QCD (solid). Using the PPR, we cover the $\cos\theta^* < 0.96$ range.

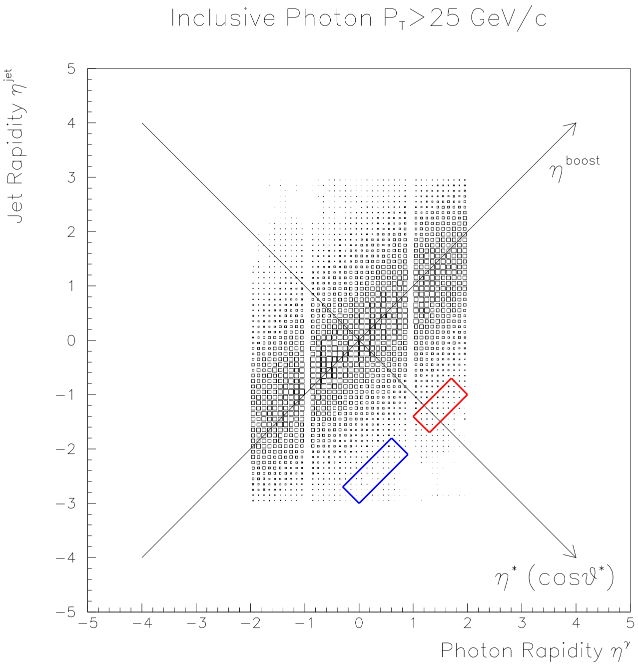

Figure 13: Scatter plot of photon and jet rapidities. The boxes represent unbiased areas for $\cos\theta^*$.

central. In this measurement, we have to reduce the total uncertainty smaller than 5% to give a constraint among the different gluon PDF's. Control of the systematic uncertainty will become more important in this regard.

5.2.2 Photon+Charm Production

CDF has made the first measurement of the photon+charm cross section with the Run IA data (17 pb^{-1}) [10]. The energy range was $16 \le E_T^\gamma \le 40$ GeV, where the lower and upper bound are due to a trigger requirement and the limitation of the γ-π^0 separation using the shower max detector, respectively. Measurements of the photon+charm production allows the direct measurement of the charm quark distribution of the proton [11]. The ratios of measurement over PYTHIA (LO) cross section are summarized in Figure 19, where electron, muon or $D^{*\pm}$ are used for charm identification. The analysis was limited by statistics ($\simeq 40\%$ uncertainty for the D^* channel) and rapidity range ($|y^\gamma| < 0.9$, $|y^c| < 1$). The production is also interesting as a QCD test in inclusive two specified particle states, for example, the rapidity correlation of photon and charm [12]. The measurement of the photon+charm cross section provides important inputs to the production cross section estimates for the current and future high energy hadron colliders. There is a new physics

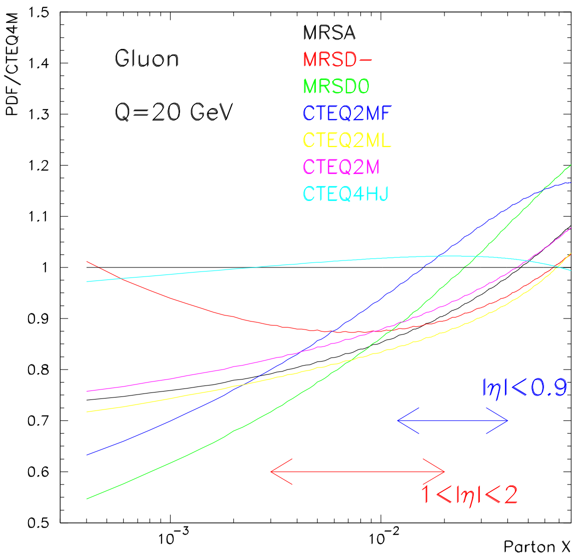

Figure 14: Various gluon distribution functions compared with CTEQ4M and x regions covered by the prompt photon production.

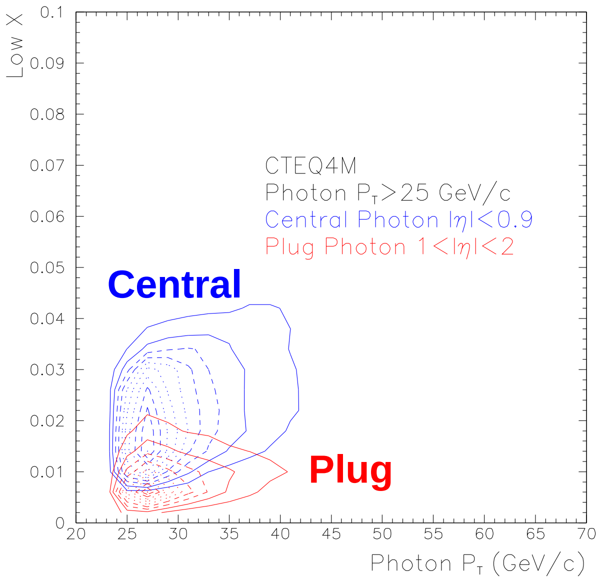

Figure 15: Kinematical map (lower x of initial partons vs. photon p_T) for the prompt photon production.

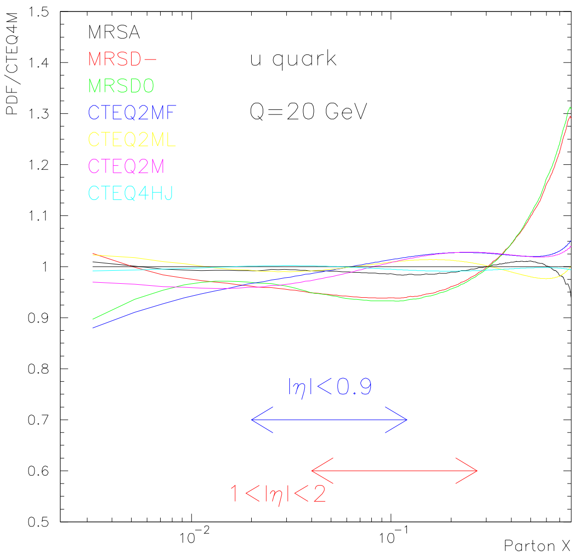

Figure 16: Various quark distribution functions compared with CTEQ4M and x regions covered by the prompt photon production.

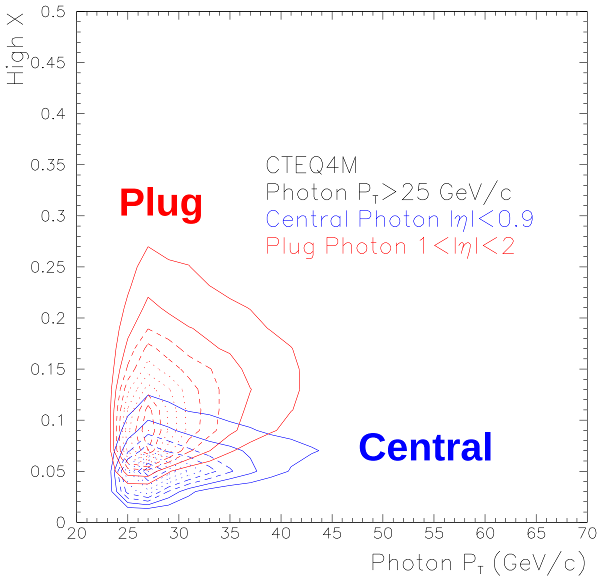

Figure 17: Kinematical map (higher x of initial partons vs. photon p_T) for the prompt photon production.

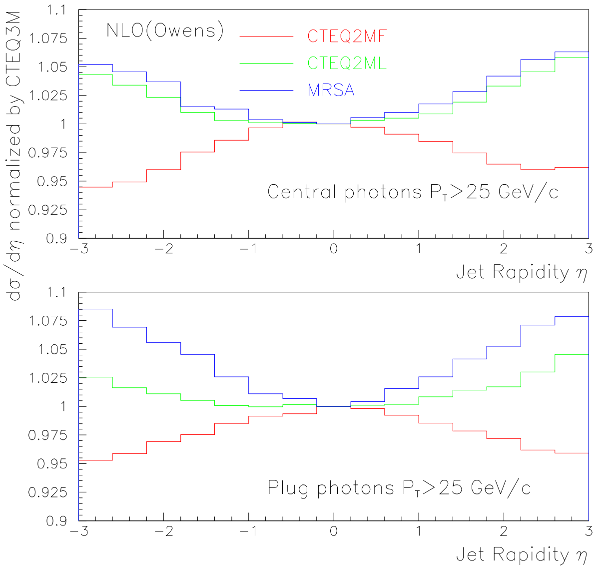

Figure 18: Jet rapidity distribution in prompt photons ($p_T > 25$ GeV$/c$) from the NLO (Owens) calculation with various PDF's.

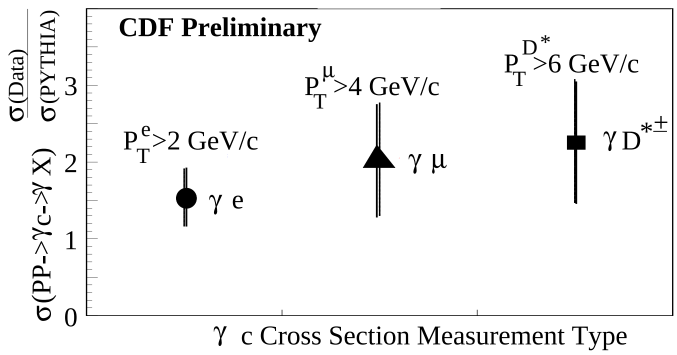

Figure 19: Ratios of measured over PYTHIA (LO) γ+charm($\rightarrow e$X, μX, or $D^{*\pm}$X) cross sections.

containing charm quarks in the final state, for example, $\tilde{t} \rightarrow c$ LSP. The photon+charm events will provide us a detail study of charm quark identification, because there is a sizable charm component in direct photon events with small bottom contribution, which is another motivation. By including plug photons, the statistics gain is a factor of 2 (see Figure 11) and a total of $\simeq 5 \times 10^5$ photon+charm events before the charm taggings will be expected in Run II data for $E_T^\gamma > 25$ GeV. Specifically, the statistical uncertainty for the D^* tagging will be $\simeq 10\%$ with the central photons only and $\simeq 7\%$ with including the plug photons.

5.2.3 Diphoton Production

The diphoton production has been studied using Run I central-central photons. Although the measured cross section is well described with a NLO prediction, the transverse momentum (k_{T}) of the diphoton system showed disagreement with the prediction [13]. This discrepancy in the k_{T} distribution might be understood by including soft gluon radiation effects in the production (see Figure 20). In Run I, this study was also restricted by statistics ($\simeq 35\%$ uncertainty) and acceptance ($|y^\gamma| < 0.9$). By including the plug photons, we can extend the rapidity ranges of two photons from $|y^\gamma| < 0.9$ to $|y^\gamma| < 2.0$, and increase the statistics by a factor of 3. This wider acceptance will enable us to perform precise measurements such as $\cos\theta^*$ and to study production properties.

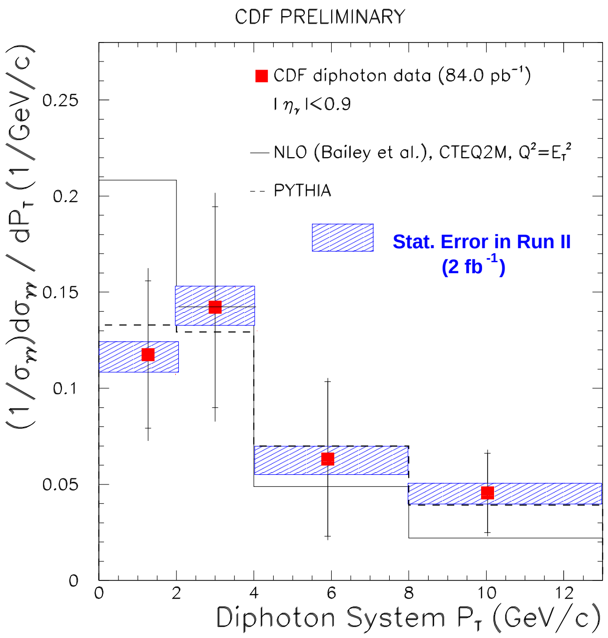

Figure 20: Transverse momentum (k_T) distribution for the diphoton system is compared with NLO QCD (solid) and PYTHIA LO (dashed), where PYTHIA includes soft gluon radiations from initial partons. We also show the expected statistical uncertainties as shaded boxes in this plot.

5.2.4 $b\bar{b}$ Correlation

The $b\bar{b}$ production in a forward region provides a constraint on the gluon PDF in a high x region (Figure 21) as well as a comparison with QCD NLO calculations. Study of the gluon PDF in a high x region is interesting because it is a check of whether the excess in the jet cross section is due to poor knowledge of the gluon distribution function.

CDF has successfully measured the $b\bar{b}$ cross section and their rapidity correlation in the forward region only using Run I inclusive forward-muon data with the SVX b-tagging of jets [14]. However, the analysis was statistically and geometrically limited as seen in Figure 22. We can add a new data point in $1 < |\eta| < 2$ by using the plug electrons in $b\bar{b}$ dilepton samples.

The plug-electron quality for the $b\bar{b}$ production process can be speculated from Figure 23 which shows the η distributions for the signal electron and isolated charged hadron background. The background distribution is the same as the one for $p_T > 12$ GeV/c already shown in Figure 9. Each signal and background distribution was normalized in the central ($|\eta| < 0.9$) region. The signal gain by the plug is 70% while the plug-to-central ratio for the background is $\simeq 1.3$. The S/N in the plug region is, therefore, $0.7/1.3 = 0.5$ times worse than that in the central.

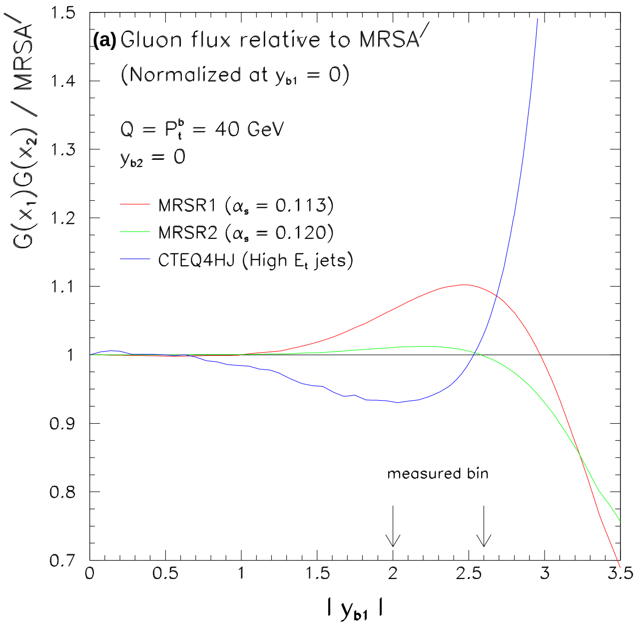

Figure 21: Comparison of the gluon flux for MRSR1, MRSR2, and CTEQ4HJ relative to MRSA' as a function of the bottom quark rapidity (y_{b1}). The curves are divided by MRSA' and normalized to unity at y_{b1}=0.

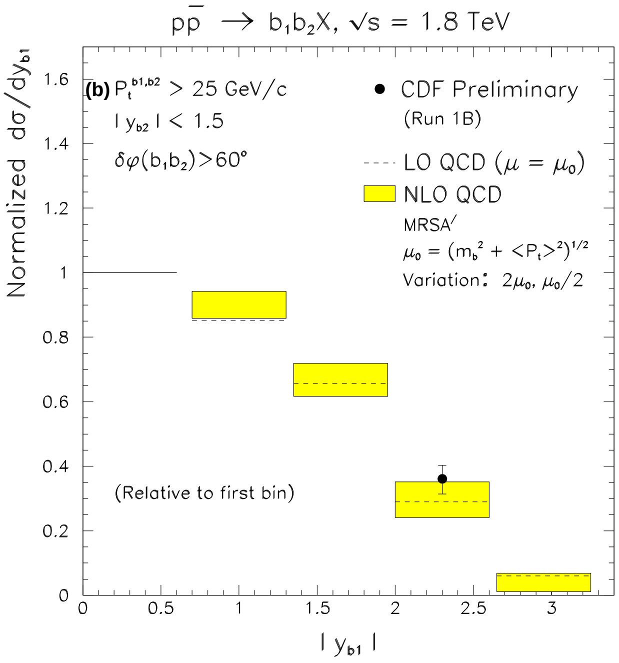

Figure 22: Central-forward $b\bar{b}$ cross section normalized to the central-central $b\bar{b}$. The filled boxes are the theory prediction in each bin taking into account of variations in the scale.

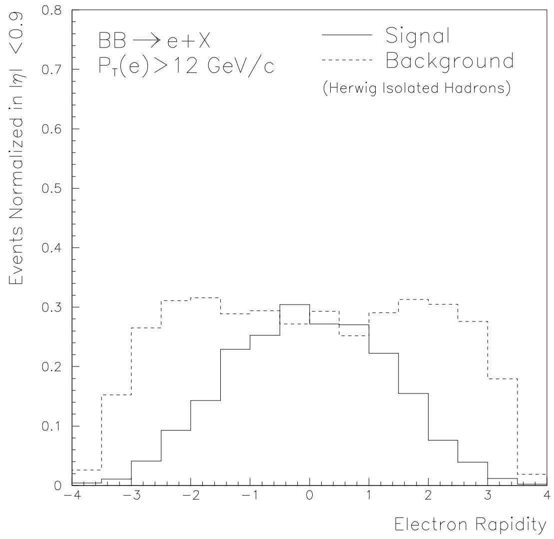

Figure 23: Pseudorapidity distributions for electrons in the $b\bar{b} \rightarrow eeX$ production (BGEN) and isolated charged hadrons (HERWIG). Each distribution is normalized in the central ($|\eta| < 0.9$) region.

5.3 Electroweak Physics

5.3.1 $W\gamma$

Studying the trilinear gauge boson couplings is one of important tests of the Standard Model. The radiation amplitude zero predicted by the Standard Model is an example of such tests for the $W\gamma$ production. In Run I, the kinematical range of the photons was restricted in the central region, and the statistical uncertainty was 30%. The photon fraction was 50% in this sample. A plug photon analysis is underway, however, the main difficulty is the background estimation without a preshower detector. Extending the acceptance of photons to the plug region using the γ-π^0 separation with the PPR, the statistics will increase by a factor of 2. Furthermore, including electrons in the plug region, the statistics will increase finally by a factor of 3. Figure 24 shows the photon production angle ($Q_W \times \cos\theta^*_\gamma$) distribution. The increased acceptance will provide us more significant radiation amplitude zero as seen in Figure 25.

5.3.2 W Asymmetry

The W charge asymmetry measurement strongly constrains the u/d quark distributions ($0.006 < x < 0.34$), and with the results of the measurement we were able to reduce the uncertainty ($\simeq 20$ MeV/c^2) on the W mass due to the PDF's in Run I analysis [15]. Figure 26 shows the measurement of the lepton charge asymmetry in W decays. In this asymmetry measurement, electrons in the plug region played an important role. The large systematic uncertainty of the asymmetry measurement (2%) comes from the electron misidentification of QCD jets. We estimated the S/N for the plug electrons from W decays with respect to the central electrons. Figure 27 shows the η distribution for $W \to e\nu$ electrons and isolated charged hadrons. The S/N relative to that in the central is 0.7.

Given much higher statistical samples possible in Run II, the systematics due to the background may become relatively large. The reduction and estimation of the backgrounds are important by using the PPR information. The e-π separation technique using the PPR will reduce the systematics to $\simeq 1\%$ as was the case for the central electrons with the CPR.

5.3.3 Drell-Yan

The low mass Drell-Yan cross section is sensitive to the PDF in a low x region which has never been explored before at Tevatron. The low mass cross section was measured [16], but the rapidity range was restricted within the central region ($|y^e| < 0.9$) and the statistics was small ($\simeq 6.7\%$ uncertainty around $M_{ee} = 20$ GeV/c^2) using Run I central electron data as shown in Figure 28. The main difficulty in this measurement is the estimation of QCD backgrounds. The S/N in the plug relative to the central is estimated to be 0.8 from Figure 29. Sample purity is, therefore, expected to be similar to the central region without the PPR, although the PPR still provides another handle to reduce the systematic uncertainty due to the QCD background. In Run II, the geometrical acceptance (a factor of 2.8, see Figure 30) and integrated luminosity will increase, and the access into unexplored low x regions will be possible with 1% statistical uncertainty.

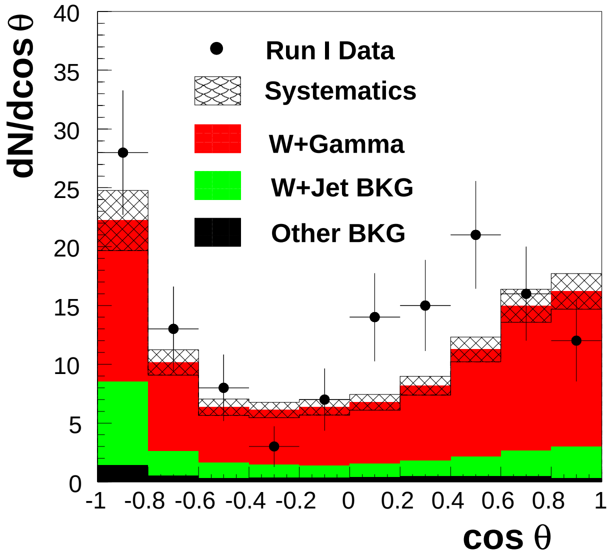

Figure 24: $Q_W \times \cos\theta^*$ distribution for the $W(\rightarrow e\nu)\gamma$ production from Run I data together with the expectation of the Standard Model and estimated background (W+Jet, τ+X, ...) contributions.

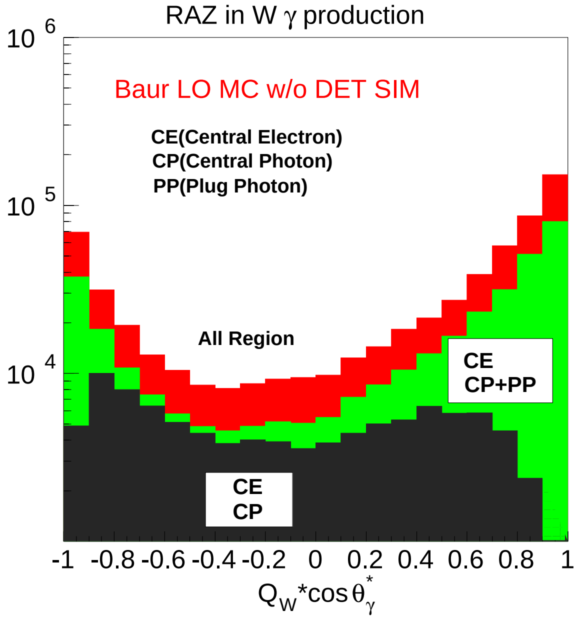

Figure 25: Expected $Q_W \times \cos\theta^*$ distributions for central electron and central photon events, central electron and plug photon events and all events generated by the Baur LO Monte Carlo generator.

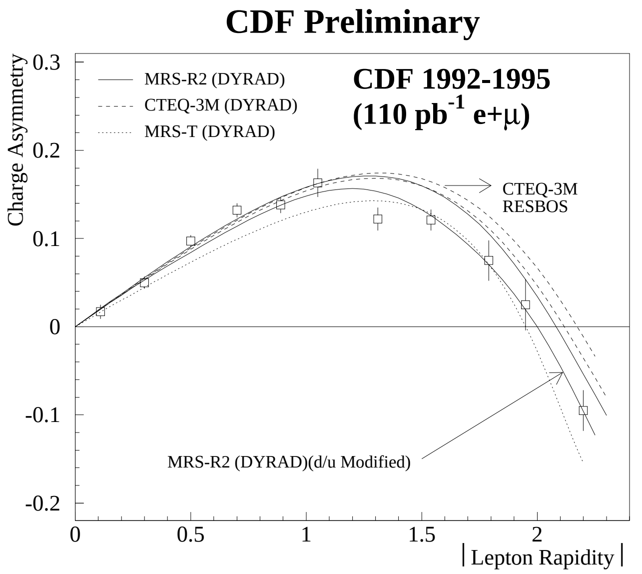

Figure 26: Run I measurement of the W charge asymmetry compared with NLO calculations with several sets of PDF's as input.

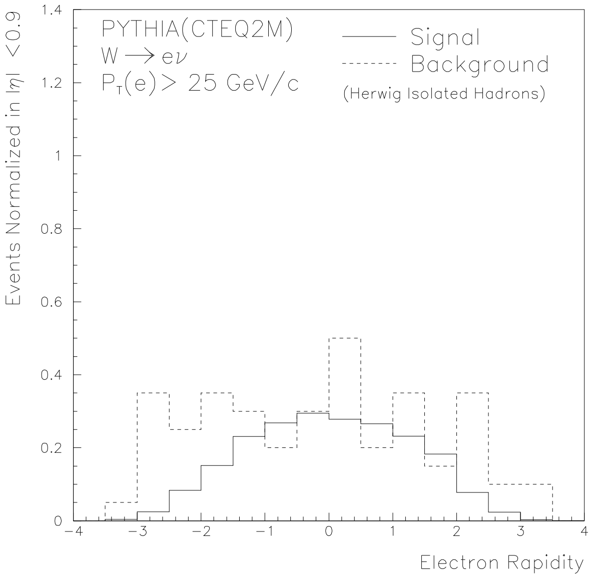

Figure 27: Pseudorapidity distributions for W decay electrons and isolated charged hadrons (HERWIG). Each distribution is normalized in the central region.

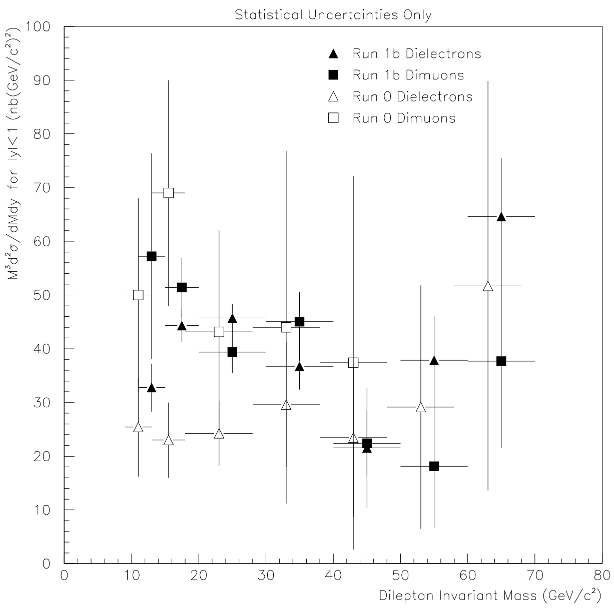

Figure 28: Drell-Yan cross sections scaled by M^3 in $10 < M < 70$ GeV/c^2 below the Z^0 mass region using Run 0, Run IA and Run IB data. Only statistical uncertainties are included in the Run IB preliminary results.

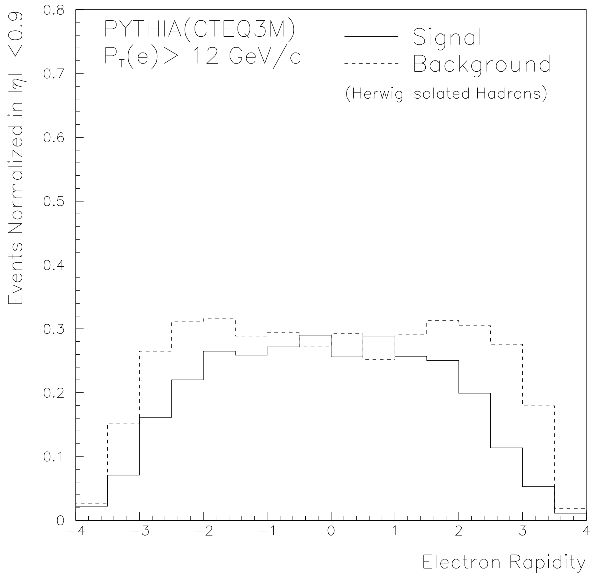

Figure 29: Pseudorapidity distributions for electrons in Drell-Yan production and charged hadrons in QCD. Each distribution is normalized in the central region.

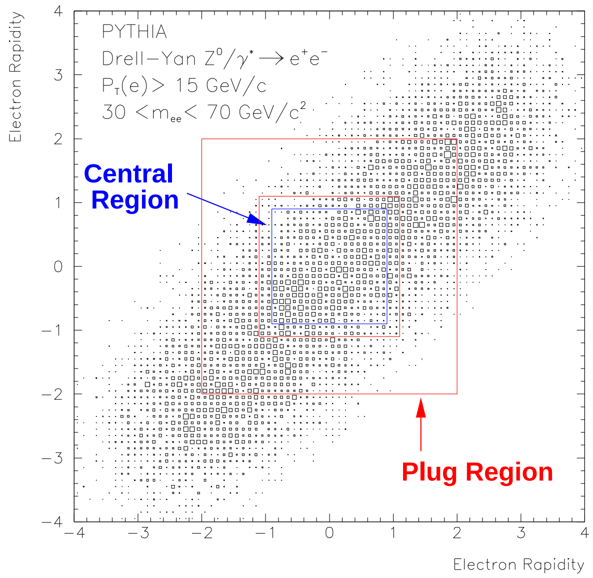

Figure 30: Scatter plot of two electron rapidities in the Drell-Yan production generated by PYTHIA. Both electrons are required to be $p_T > 15$ GeV/c and $20 < m_{ee} < 70$ GeV/c^2.

5.4 Top Quark Physics

The observation of the top quark production has opened a new field of the top quark physics. In Run II, we will have an opportunity to study the top quark characteristics precisely with high statistics data samples. In the Run I lepton+jet analysis, the lepton (electron) rapidity was restricted in the central region because of a large background fraction in the plug electrons.

5.4.1 $t\bar{t}$ Production

By using data with electrons detected with the plug calorimeter, we might expect a significant increase of the acceptance and the kinematic range of the $t\bar{t}$ production and decays. In this section we focus on the $t\bar{t} \to e^{+}$+jets channel.

We have generated $t\bar{t}$ events for a top quark mass of 175 GeV/c^2 with the HERWIG Monte Carlo program. The analysis has been performed using GENP-level data; neither a detector simulation nor trigger simulation was processed. The t and $\bar{t}$ quarks were completely reconstructed with their decay products, and we selected only events in which t and $\bar{t}$ respectively decays as follows:

$$\begin{aligned} \bar{t}\,t \quad &\to \quad (W^{+}b)\ (W^{-}\bar{b}) \\ W^{+} \quad &\to e^{+}\nu \\ W^{-} \quad &\to q\bar{q}'. \end{aligned}$$

To simulate the basic event selection, we applied the following requirements:

$$p_T^{e^+} \geq 20 \text{ GeV}/c, \qquad |\not{p}_T| \geq 20 \text{ GeV}/c,$$

where $p_T^{e^+}$ is the transverse momentum of e^+ and $\not{p}_T$ is the vector sum of the transverse momenta of the visible particles (i.e. e^+, b, $\bar{b}$, q, $\bar{q}'$). We further required the quarks (b, $\bar{b}$, q, $\bar{q}'$) to satisfy the following criteria on the transverse momentum and pseudorapidity:

$$p_T^{qrk} \geq 15 \text{ GeV}/c, \qquad |\eta^{qrk}| \leq 2.$$

Acceptance Increase

Shown in Figure 31 is the positron η distribution. The open and the hatched histograms correspond to the positron η range of $|\eta| \leq 1$ (central) and $1 \leq |\eta| \leq 2$ (plug), respectively. From this comparison, we estimated the gain in the electron detection with the plug detector to be 30%.

We also checked the acceptance increase for electrons from $t \to b \to e$ decays by inclusion of the plug. We first restricted the η range of e^+ from W^+ which came from the t decay to $|\eta| \leq 2$ and then selected events which have an electron or positron from the b or $\bar{b}$-quark semileptonic decay. The electron (or positron) was required to have the transverse momentum greater than 3 GeV/c. We show the electron η distribution in Figure 32. The gain was estimated to be 28%. We summarize the results in Table 4.

Kinematic Range

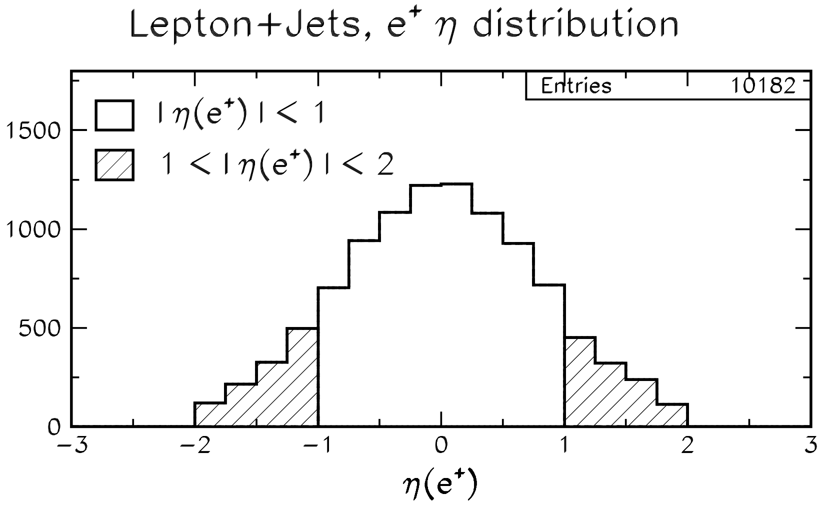

Figure 31: Positron η distribution for $t\bar{t}$ (lepton+jets) events.

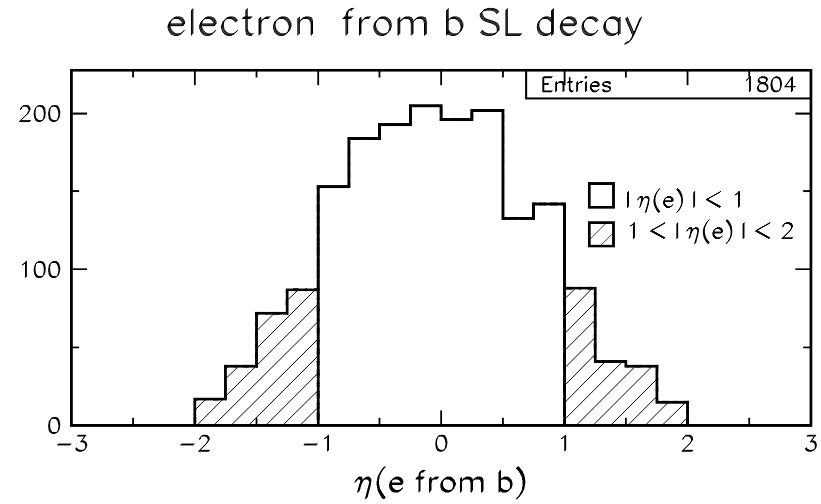

Figure 32: Pseudorapidity distribution for e^- (or e^+) from the b (or $\bar{b}$) semileptonic decay in $t\bar{t}$ (lepton+jets) events.

$t \to W \to e$	
η region	ratio
$0 < \lvert\eta\rvert < 1$	1
$1 < \lvert\eta\rvert < 2$	0.29

$b \to e$	
η region	ratio
$0 < \lvert\eta\rvert < 1$	1
$1 < \lvert\eta\rvert < 2$	0.28

Table 4: Ratios of $t\bar{t}$ events with a plug electron to those with a central electron are listed for $e^{\pm}$ from $W^{\pm}$ coming from the t or $\bar{t}$ decay (left) and $e^{\mp}$ from the b or $\bar{b}$ decay (right).

We will show the distributions of several quantities which might help us understand the kinematic properties of $t\bar{t}$ production and decays. The variables we look at are:

(i) $p_T^{t\bar{t}}$: transverse momentum of the $t\bar{t}$ system.

(ii) $y_{t\bar{t}}$: rapidity of the $t\bar{t}$ system.

(iii) p_T^t: top-quark transverse momentum.

(iv) y_t: top-quark rapidity.

(v) $\cos\theta_t^*$: top-quark scattering angle in the $t\bar{t}$ rest frame.

(vi) $\cos\theta_{e^+}^*$: lepton helicity angle, which probes the polarization state of the W and can be measured in the lab frame as $\simeq 2M_{eb}^2/(M_{eb\nu}^2 - M_W^2) - 1$.

We simply compare the distributions of the kinematical variables for events with e^+ in the central region and for events with e^+ in the plug region in Figures 33 and 34. The distributions of $\cos\theta_t^*$ and y_t show that the detection of the plug electron slightly expands its acceptable region. For the other variables, we do not see any significant increase of the kinematical regions of interest.

S/N for Electrons in the Top Events

We estimated the S/N for electrons in the $t\bar{t}$ production using the HERWIG generator. Figure 35 shows the η distributions for $W \to e\nu$ and $b \to eX$ electrons in the $t\bar{t}$ production. The S/N in the plug region is worse than the central by a factor of 3 for both the $W \to e\nu$ and $b \to eX$ electrons.

The SLT b-tagging in Run I includes the e-π separation using the CPR. Since the CPR and PPR performances of the e-π separation are similar, the SLT tagging in the plug using the PPR will have a similar efficiency for the electrons and a reduction for the background. Thus, the relative rate between the signal and the background shown in Figure 35 determines the S/N. The fact that the S/N in the plug is worse by a factor of 3 compared with the central means that the S/N for SLT samples in the plug region is bad that much compared with the central even after applying the e-π separation by the PPR to the plug electrons from b decays. In Run II, the SVX b-tagging will be significantly improved by the extension of the SVX II coverage and the improved tracking efficiency,

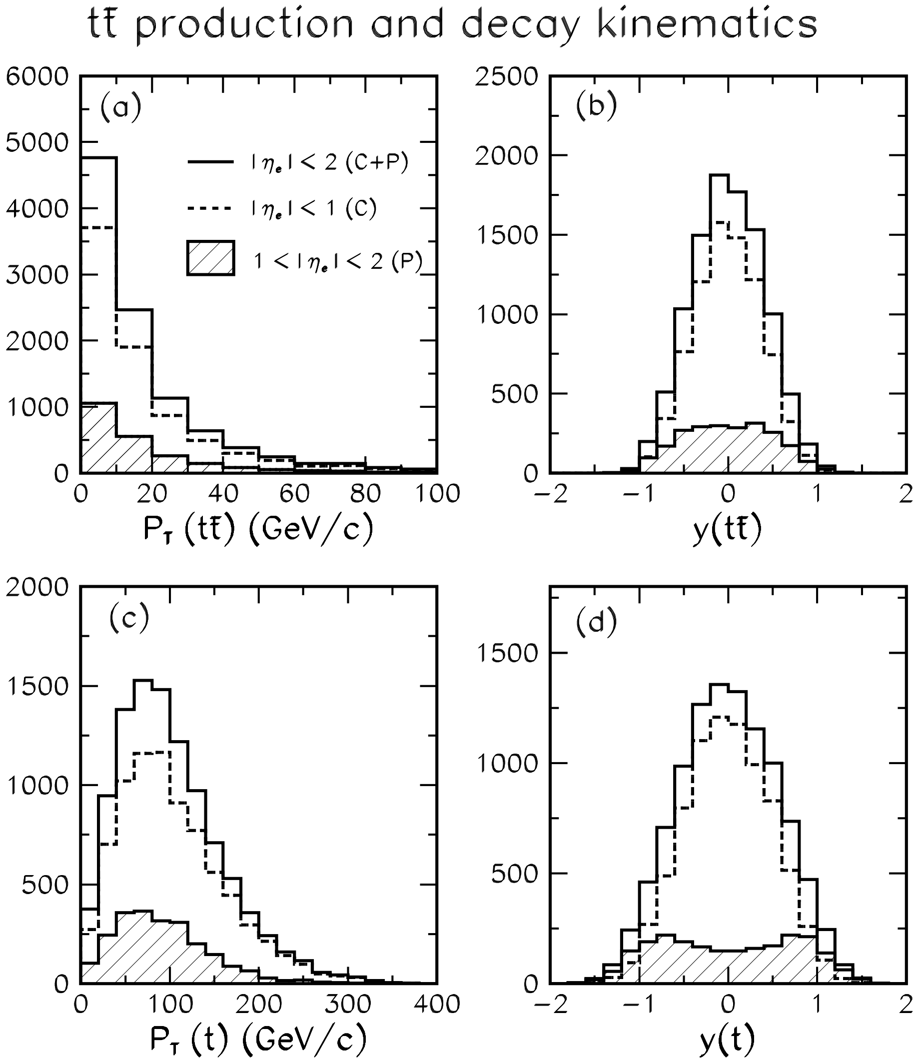

Figure 33: Distributions of the kinematical variables: (a) $p_T^{t\bar{t}}$, (b) $y_{t\bar{t}}$, (c) p_T^t, and (d) y_t.

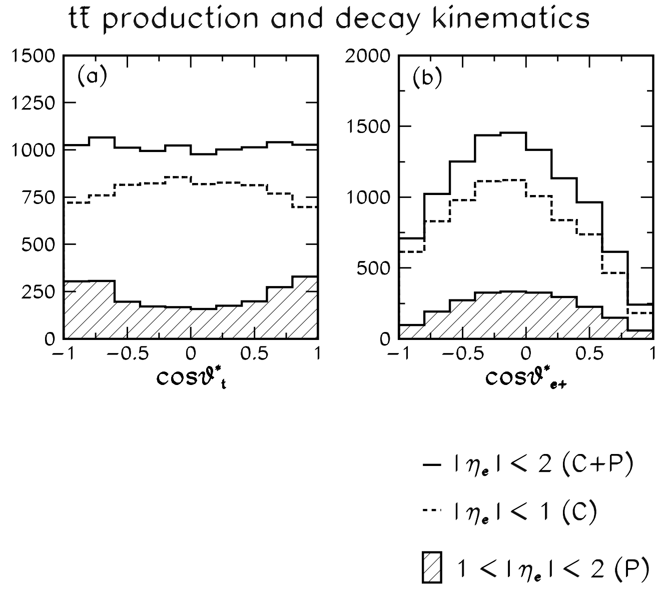

Figure 34: Distributions of the kinematical variables: (a) $\cos\theta^*_t$ and (b) $\cos\theta^*_{e+}$.

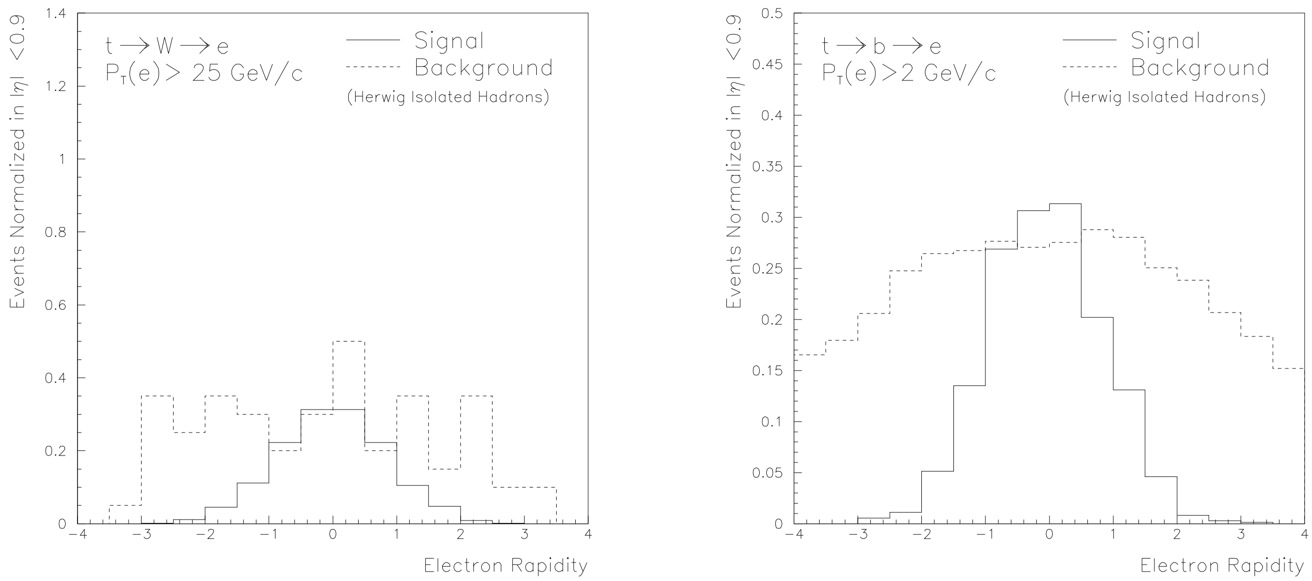

Figure 35: Pseudorapidity distribution for $W \to e\nu$ and $b \to eX$ electrons in the $t\bar{t}$ production, where each distribution is normalized in the central region.

thus the SLT tagging itself will become less important than the SVX tagging [17]. Although the inclusion of the SLT tagging in the plug region gives you a 30% gain within the SLT tagging for the electrons, it will not help the b tagging in the top events because of the small acceptance on the whole and the low S/N.

5.4.2 t-W-b Coupling (W Helicity)

We expect that new physics might present a new non-universal top interaction at its mass scale [18]. A W helicity measurement using Run I data is underway, and the preliminary results of the longitudinal W fraction in top decays are obtained with the statistical uncertainty of 55% [19]. The measurement is limited by statistics. The increased statistics in Run II will provide precise information of the top quark decay. The largest systematic uncertainty in this measurement comes from the QCD background estimation. The reduction and understanding of the QCD backgrounds is one of the best way to reduce the systematics. The PPR can be used for this aim in the analysis with the plug electrons. The uncertainty on the longitudinal W fraction will be reduced to 5.5% using 2 fb^{-1} data [1].

5.4.3 Single Top Production

The single top productions via $qq \to tb$ (W^* production) and $qb \to qt$ (W-gluon fusion) are related to the top quark decay width and the CKM matrix element $|V_{tb}|^2$. The predicted cross sections of these processes are 0.7 pb (W^*) and 1.7 pb (Wg fusion) at a top mass of 175 GeV/c^2 [20]. An upper limit of the cross section for the W-gluon fusion production was obtained using Run I data [21]. The acceptance will be increased by a factor of 1.5 including electrons in the plug region, which will provide us a cross section measurement with 20% statistical uncertainty.

5.5 B Physics

We have generated $B\bar{B}$ events with the BGEN+CLEO Monte Carlo program. We used $B\bar{B} \to e^+e^-X$ and $B\bar{B} \to \psi(\to \mu\mu)K + eX$ events in this analysis.

Acceptance Increase

We first consider the acceptance increase in dilepton analyses. We require both the electrons to have $p_T > 2$ GeV/c. Shown in Figure 36 is the electron η distribution for the events with e^+ in the central region ($|\eta| < 1$). We can expect roughly 120% or more events by including the plug region than using only the central detector. However, we need a trigger-level tracking in the plug region for dilepton samples involving plug electrons.

We then estimate the acceptance increase for central lepton inclusive samples. We require e^+ with $p_T^{e^+} > 12$ GeV/c to be in the central region and look at the η distribution for the opposite electron (see Figure 37). The gain is about 60% by including the plug detector for the b detection, however, the amount of the expected events for this sample is only $\simeq 1$% of the previous sample ($p_T^{e^+}$, $p_T^{e^-} > 2$ GeV/c and both in the central). We summarize the results in Table 5.

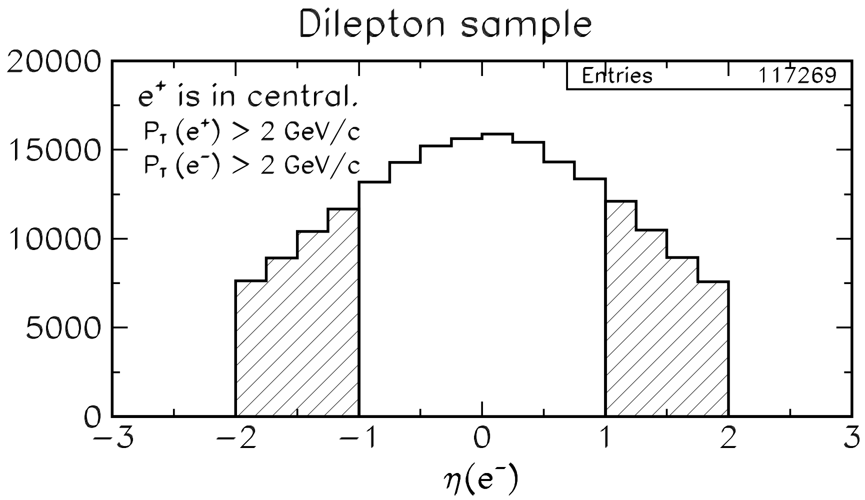

Figure 36: Pseudorapidity distribution for e^- from the b semileptonic decay in $B\bar{B}$ events. The other electron (e^+) from $\bar{b}$ is required to be in the central region.

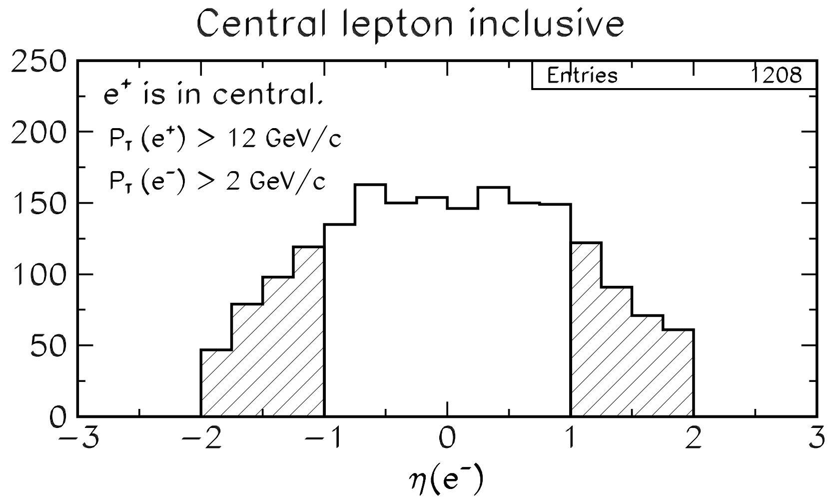

Figure 37: Pseudorapidity distribution for e^- from the b semileptonic decay in $B\bar{B}$ events. The other electron (e^+) from $\bar{b}$ is required to be in the central region and to have $p_T > 12$ GeV/c.

e^+	e^-	ratio
central	central	1
central	plug	0.66
plug	central	0.66
plug	plug	0.52

e^+	e^-	ratio
central	central	1
central	plug	0.57

Table 5: Ratios of $b\bar{b}$ events with a pair of central-central electrons to ones with central-plug and plug-plug electrons. Left: dilepton sample ($p_T(e^{\pm}) > 2$ GeV/c) and right: central e inclusive sample ($p_T(e^+) > 12$ GeV/c).

In $B\bar{B} \to \psi(\to \mu\mu)K + eX$ channel for the opposite side B tagging, we show the electron p_T in the plug region and the rapidity distributions in Figure 38, where the muons from ψ decay are restricted within $|\eta^\mu| <2$ and $p_T^\mu > 2$. The acceptance increases by a factor of 1.7 including plug electrons ($p_T >2$ GeV/c).

S/N for Electrons in the $b\bar{b}$ Production

We estimated the S/N in electron candidates (triggered electron $p_T > 12$ GeV/c, b-tagging soft electron $p_T > 2$ GeV/c) from the $b\bar{b}$ production. Figure 39 shows the η distributions for electrons in the $b\bar{b}$ production (BGEN) and isolated charged hadrons from QCD (HERWIG). The S/N's in the plug region are worse than the central by a factor of 2 for the trigger and soft electrons in the $b\bar{b}$ production.

Kinematic Range

In measurement of the differential cross-section of the $B\bar{B}$ production $d\sigma(b)/d\eta$, we can expand the kinematical region by including plug electrons. We require events to have e^+ with $p_T > 12$ GeV/c. Figure 40 shows the η distribution for $\bar{b}$; the open histogram is for events with e^+ in the central region ($|\eta| < 1$) and the hatched histogram is for ones in the plug region ($1 < |\eta| < 2$), respectively. Because of the correlation of the e^+ direction to the one of its parent quark, the acceptable η region can be expanded up to $|\eta| \simeq 2$.

5.6 Summary

It has been shown that the plug region has potential to make a significant contribution to the photon physics in accessing kinematically extended regions compared with the central region. The statistics is typically larger than the central and the statistical uncertainty in Run II will be a few % level. The PPR is necessary for the statistical separation of photons from neutral hadron backgrounds in the photon physics.

The plug electrons are also important for various physics topics. However, the S/N will be worse than that in the central as summarized in Table 6. As will be discussed in Section 6.2, the PPR provides another reduction factor of $\simeq 2$ against the hadron backgrounds. The quality of the plug electron selected with the PPR information will be

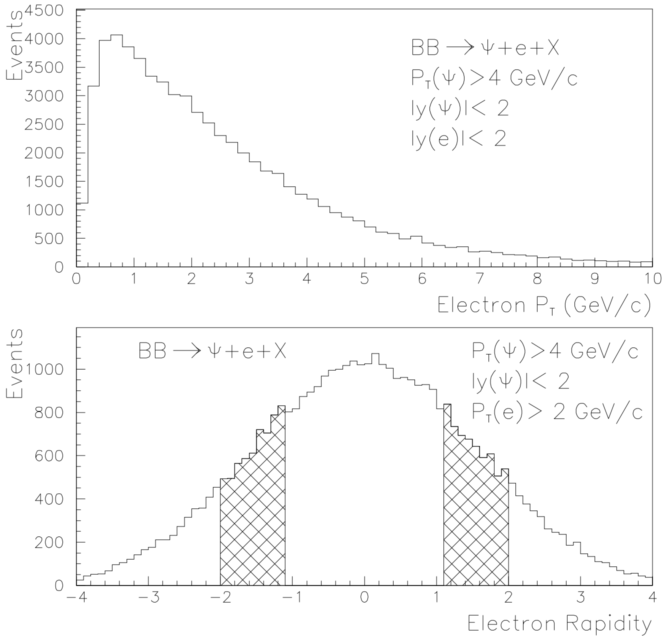

Figure 38: Distributions of p_T and η for plug electrons from the B decay in $BB \to \psi K + eX$, where muons from ψ decays are restricted within $|\eta^\mu| < 2$ and $p_T^\mu > 2$ GeV/c.

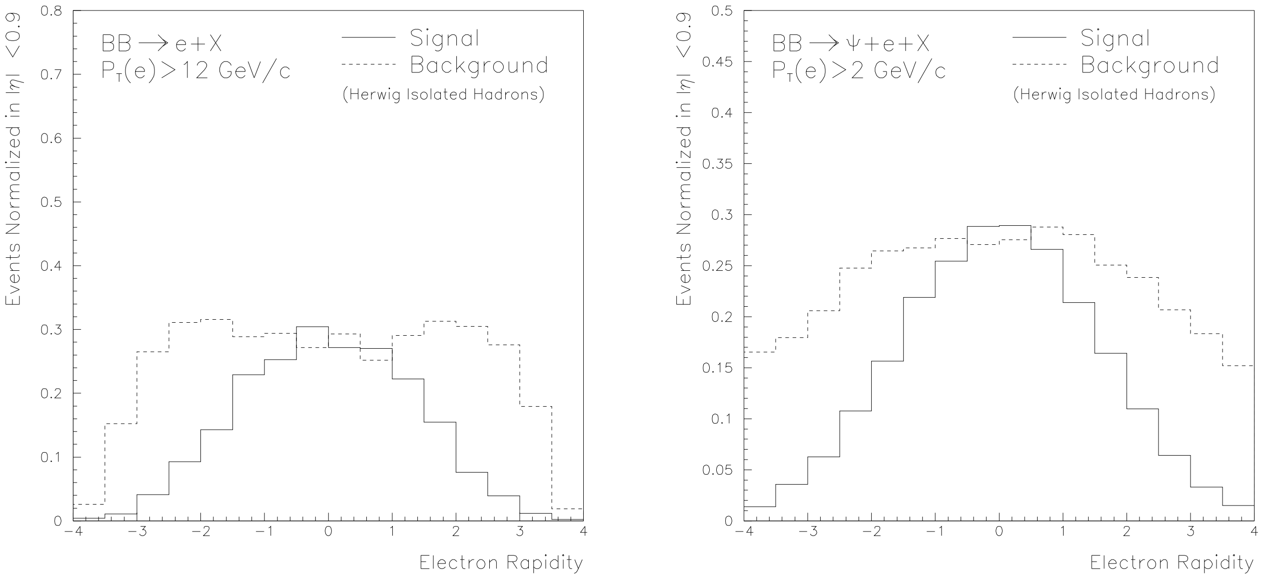

Figure 39: Pseudorapidity distributions for electrons in the $b\bar{b}$ production. Left: trigger electrons ($p_T > 12$ GeV/c), right: soft electrons for the b flavor tagging ($BB \to \psi K + eX$).

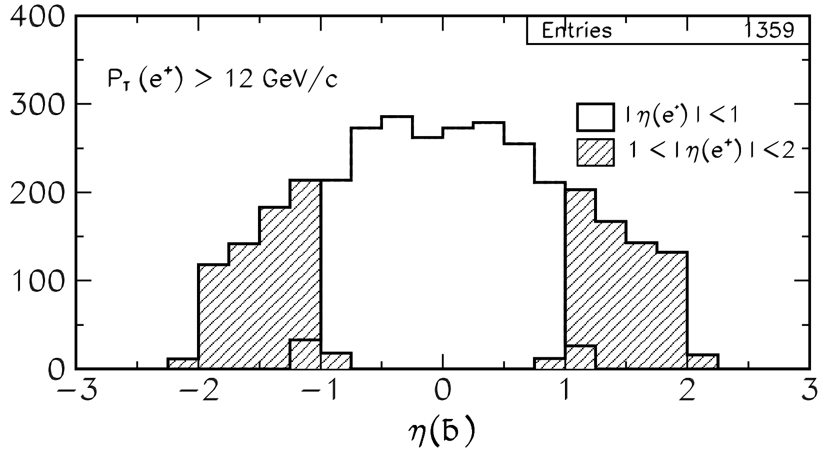

Figure 40: Pseudorapidity distribution for the $\bar{b}$ quark in $B\bar{B}$ events, where e^+ from $\bar{b}$ is required to have $p_T > 12$ GeV/c.

Source	p_T region ($p_T^{\min}$ GeV/c)	Signal Acceptance P/C ratio	BG Acceptance P/C ratio	S/N P/C ratio
Top W	25	0.3	1.0	0.3
Top b	2	0.3	1.2	0.3
Single Top (W)	25	0.5	1.0	0.5
$BB \to \psi K + e$	2	0.7	1.2	0.6
W	25	0.7	1.0	0.7
Drell-Yan	12	1.0	1.3	0.8
$b\bar{b}$	12	0.7	1.3	0.5

Table 6: Acceptance ratios between the plug and the central (P/C) for electrons from various physics sources and for the hadron background (BG), with the corresponding plug S/N's relative to the central.

similar to that of the central electron selected without the CPR information. In the case that the central electrons are selected with CPR cuts as in the SLT tagging, the S/N's in the plug region relative to the central remain the same as shown in Table 6, since the CPR and PPR have a similar e-π separation power as also given in Section 6.2. In any cases, we may need to include requirements on the PPR response in standard selection of the plug electrons in Run II.

6 Test Beam Results

We here describe test beam results of the PPR [22]. The test beam module is identical to three units ($\Delta\phi = 45°$) of the real PEM calorimeter. The PEM test beam module is followed by the plug hadron calorimeter (HAD) test beam module. As an optical

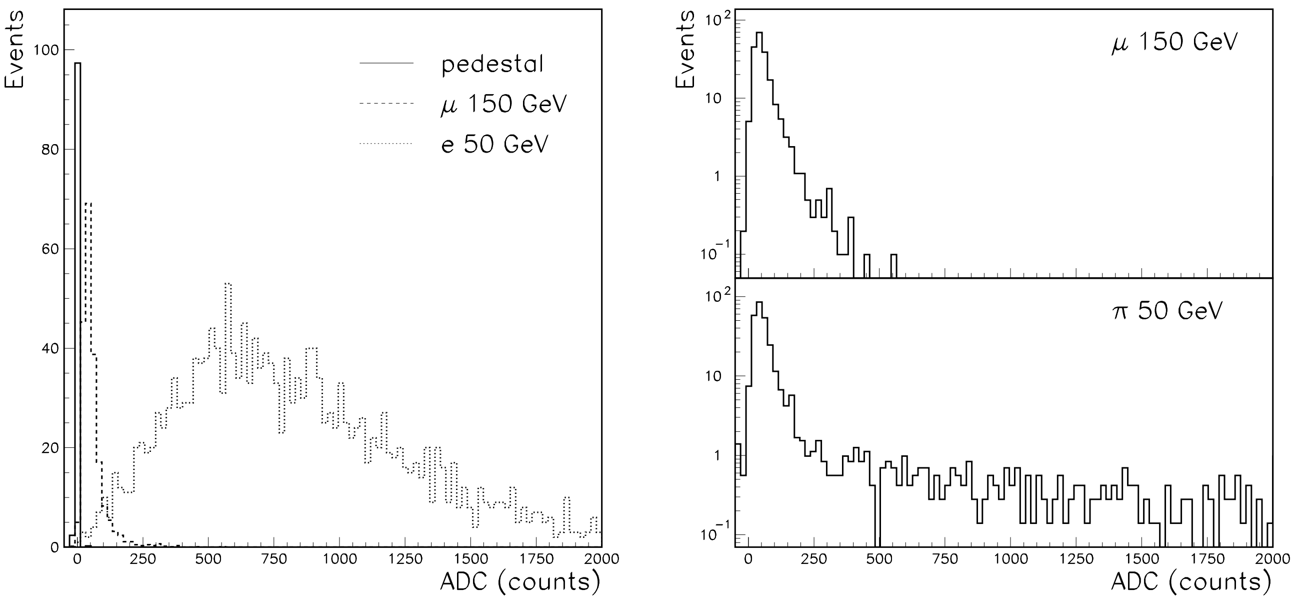

Figure 41: Pulse height distributions of the PPR for 150 GeV μ^+, 50 GeV π^+, and pedestal events in the left plot. Muons and 50 GeV π^+ are shown in the right plot. The typical light yield of the PPR is $\simeq$ 10 photoelectrons. Gain of the MAPMT is $\simeq 3.8 \times 10^5$ for this tower (the reference tower). One ADC count corresponds to 11.4 fC.

readout of the PPR tile/fiber (the first layer of the PEM), we used HAMAMATSU R5900 multianode PMT's (MAPMT's) with a gain of $\simeq 2.5\times10^5$. The efficiency of MIP detection and the e-π separation power were obtained from the pulse height distributions for e^+, π^+, and μ^+ beams with energies of 5 $\sim$ 227 GeV. The total material in front of the PPR corresponds to 1.5 X_0 including air, chamber vessels in the beam line, the front cover of the PEM, and the aluminum plate (0.43 X_0) simulating the end plate of the CDF tracking chamber.

Figure 41 shows the pulse height distributions of the PPR at a reference tower ($\eta = 1.5$, $\phi = 18.75°$) for muons, electrons, and pions.

6.1 Expected Performance of the γ-π^0 Separation

A preshower detector is required to have a high efficiency of detecting the photon conversion and a low noise fraction for an accurate determination of the photon fraction in a sample of neutral EM showers. Taking the 2 MIP's as the conversion events conservatively, we found that the PPR is > 99% efficient while keeping the noise occupancy less than 1% for the reference tower, where the pulse height distribution for 2 MIP's was artificially made by convoluting two sets of the identical 1-MIP distribution given in Figure 41. This results in a systematic uncertainty in estimation of the photon fraction less than 1%.

The efficiencies of detecting 2 MIP's for all the towers except at smaller η edge are shown in Figure 42, where the efficiency is measured for a noise occupancy lower than 1%.

The corresponding systematic uncertainties of the photon fraction are shown in Figure 8.

6.2 Expected Performance of the e-π Separation

Discrimination of charged pions from electrons is mostly done by requiring a large energy deposition in an EM part compared to HAD. However, pions interacting early in the EM section would pass a $E_{\rm HAD}/E_{\rm EM}$ (HAD/EM) cut. The use of a preshower detector can help in the recognition of these events.

The ratio of HAD energy to EM energy for 150 GeV electrons and 150 GeV pions is shown in Figure 43. A cut of HAD/EM<0.1 is $> 99\%$ efficient for electrons and $< 1\%$ for pions. Figure 44 shows the probability of a given PPR response (normalized to a MIP response) for 150 GeV electrons and pions for the events satisfying HAD/EM<0.1. Requiring the response of the PPR to be larger than 7 MIP's, for example, provides an additional reduction factor of 1.7 against charged pions while keeping 95% of the electrons as shown in Figure 45.

The same analysis was repeated for other towers. The efficiencies of the cut on the PPR signal for 50 GeV charged pions satisfying HAD/EM<0.1 are shown in Figure 46, where the cut value is chosen so as to be 95% efficient for 50 GeV electrons. Basically, the performance is similar to the reference tower. It is capable to obtain the reduction factors between $1.4 \sim 2.0$ for EM-rich charged pions by requiring an appropriately large signal in the PPR, with keeping a 95% efficiency for electrons.

Energy dependence of the PPR cut is also studied at the reference tower. In Figure 47 is shown the electron and pion efficiencies as a function of energy for a 7 MIP's cut. We see that the reduction factors are $1.7 \sim 2.3$ for the energies larger than 30 GeV, while keeping more than 90% of electrons. Rather than fixing the cut value on the PPR response, the result with varying the PPR cut value to keep $> 95\%$ efficiency for electrons at each energy is shown in Figure 48. Another useful plot is the hadron reduction vs. the electron efficiency given in Figure 49.

It is interesting to compare the CPR and the PPR performance of the e-π separation. Using the plug EM shower max detector (PES), we applied similar cuts to define interacting pions as the CPR test beam analysis [23], which were $0.1 < E_{\rm EM}/p < 0.85$ and $E_{\rm CES}/p > 0.6$. The comparison is summarized in Table 7. The PPR has a performance similar to the CPR.

Efficiency for electrons (%)	Reduction factors			
	50 GeV		10 GeV	
	CPR	PPR	CPR	PPR
90	1.6	1.5	1.8	2.0
75	2.1	1.7	2.7	2.9

Table 7: Comparison of the pion reduction factors between the CPR and PPR.

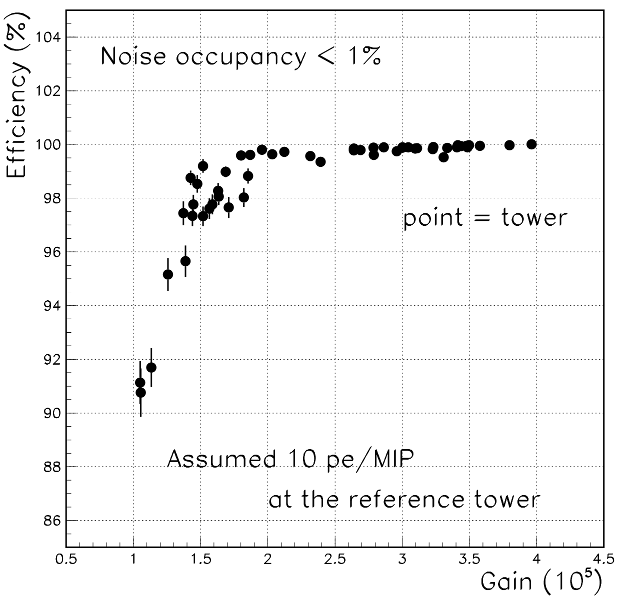

Figure 42: Efficiency of detecting 2 MIP's at the noise occupancy smaller than 1% as a function of the MAPMT gain.

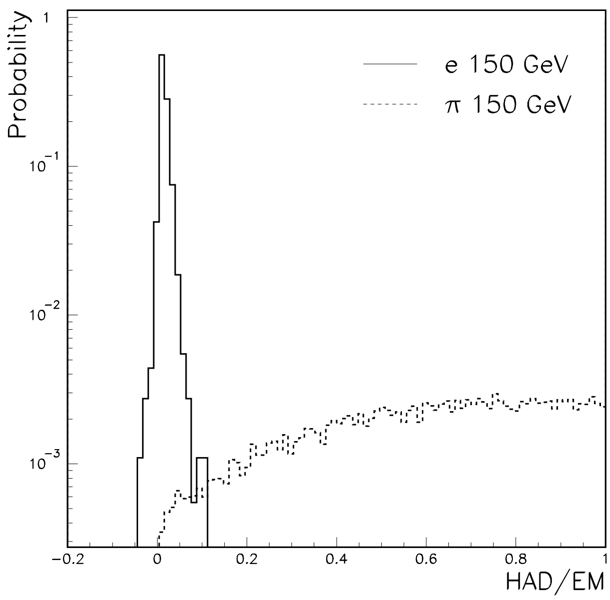

Figure 43: Ratio of electromagnetic and hadronic energy (HAD/EM) for 150 GeV e^+ and π^+ particles.

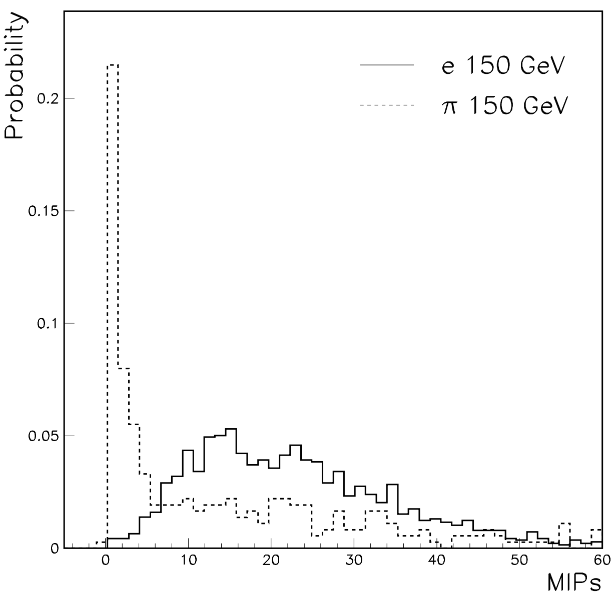

Figure 44: Response of the PPR in terms of the number of MIP's for 150 GeV e^+ and π^+ beams after the HAD/EM < 0.1 cut.

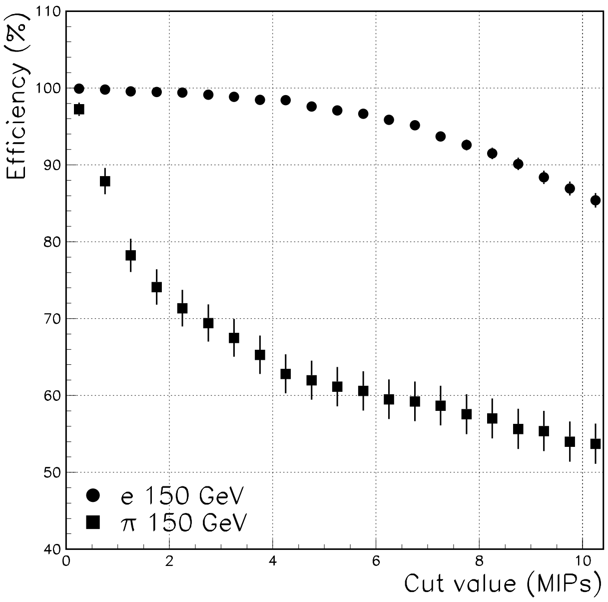

Figure 45: Efficiency for 150 GeV e^+ and π^+ particles after the HAD/EM < 0.1 cut as a function of the threshold on the PPR response.

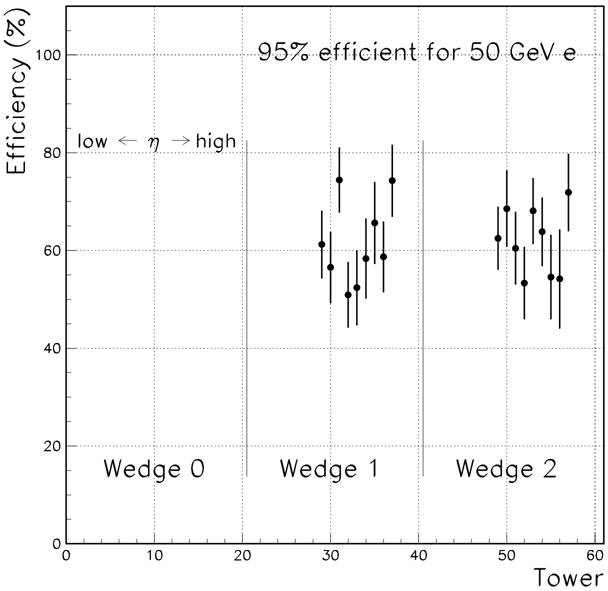

Figure 46: Efficiency of the cut on the PPR response for 50 GeV π^+ after HAD/EM<0.1 for various towers. The cut value is chosen to be > 95% efficient for e^+ of the same energy.

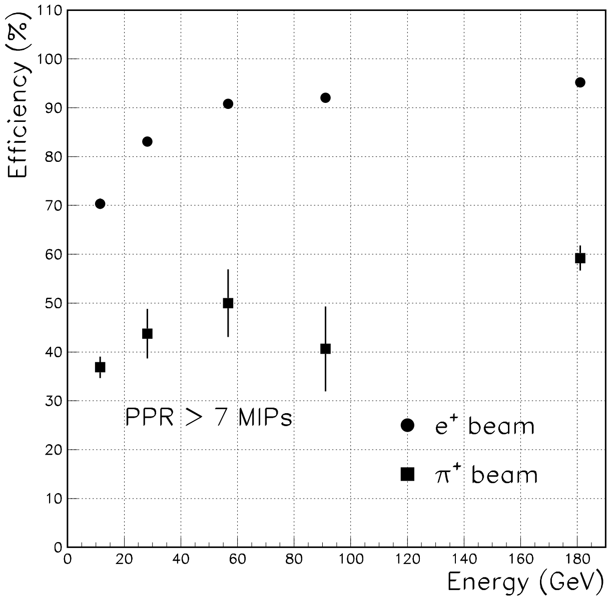

Figure 47: Efficiency of a 7 MIP cut on the PPR response for e^+ and π^+ particles after HAD/EM < 0.1 at several energies.

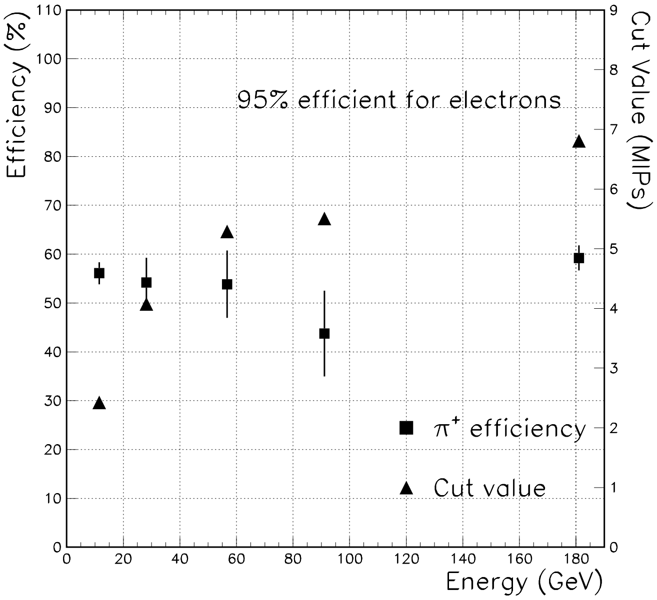

Figure 48: Efficiency of cuts on the PPR response for π^+ particles after HAD/EM<0.1 at several energies. Cuts are chosen to be > 95% efficient for the e^+ particles at each energy. The cut values are also shown.

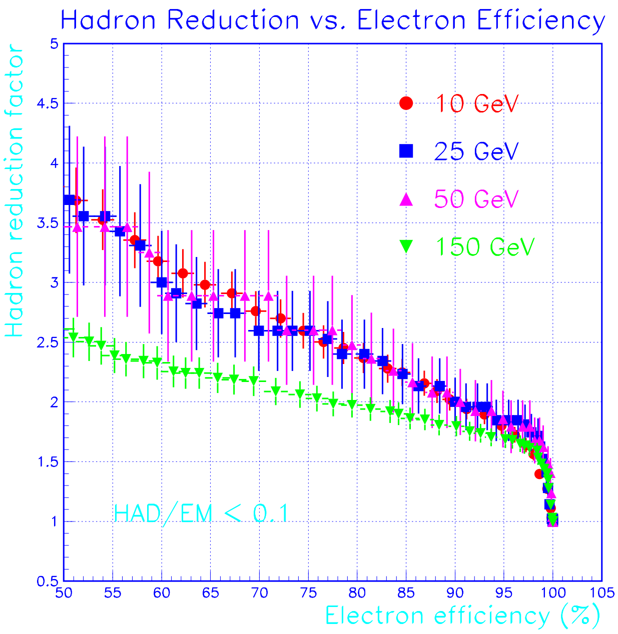

Figure 49: Hadron reduction factor vs. electron efficiency for the PPR.

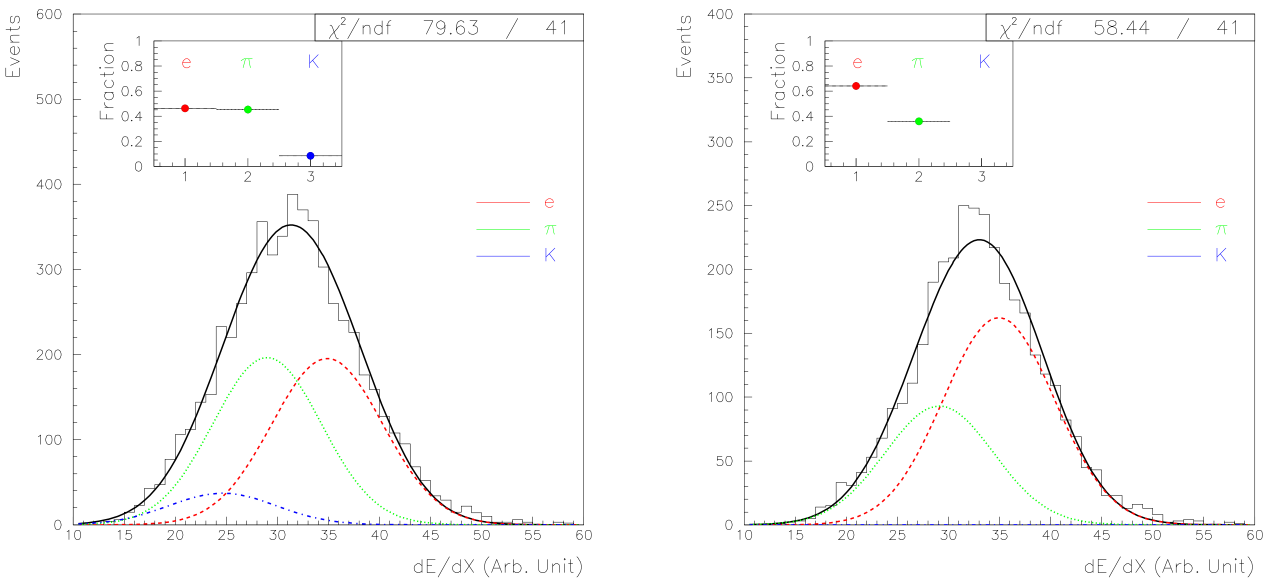

Figure 50: Distributions of dE/dx (in arbitrary unit) for the soft electron candidates in the Run I inclusive electron ($p_T > 12$ GeV/c) sample before (left) and after (right) the CPR pulse height cut.

We also estimated the e-π separation power of the CPR in the soft electron b-tagging. We calculated the electron fraction in a SLT sample ($2 < p_T < 5$ GeV/c) using dE/dx distributions shown in Figure 50. The SLT sample was collected in the inclusive electron sample ($p_T > 12$ GeV/c). The requirements on the SLT sample are identical to those in the top quark analysis (C$TOP:LOWELE.CDF) [24] except that the CPR pulse height cut is removed. Applying the CPR pulse height cut, the electron fraction increases to 67% from 49%, that corresponds to a reduction factor of 2 with $\simeq$ 80% electron efficiency. The PPR performance with the SLT selection from the test beam data is shown in Figure 51. Again, the PPR is similar to the CPR.

Overlap of neutral and charged hadrons is another source of the electron background. In the case that the momentum resolution in the plug region is worse than that in the central, the contribution of this background to the electron candidates will become different. Using the same dE/dx technique, we checked how the overlap background affects the soft electron identification. We simulated the worse momentum resolution by adding a $\Delta p_T/p_T^2 = 5\%$ smearing to measured p_T of soft electron candidates in $0 < E/p < 2$, and applied the SLT selection. The hadron reduction and the electron efficiency did not change within errors, but a $\simeq 5\%$ decrease of the final electron statistics was seen.

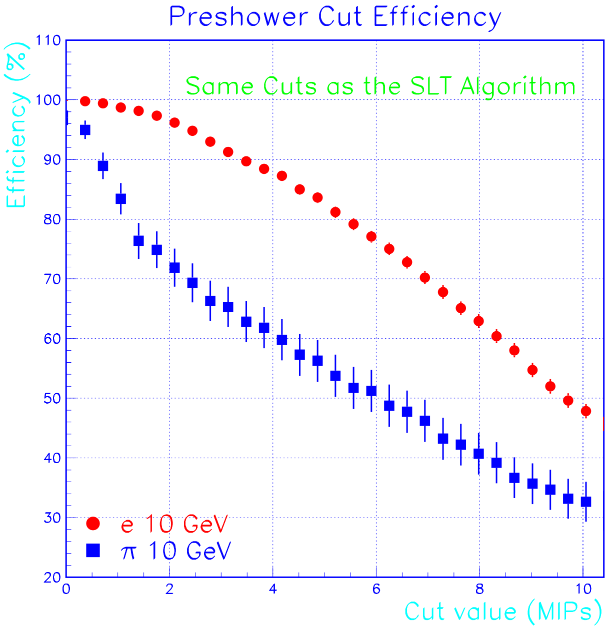

Figure 51: Efficiencies of cuts on the PPR response for 10 GeV e^+ and π^+ that satisfy the selection similar to the SLT algorithm.

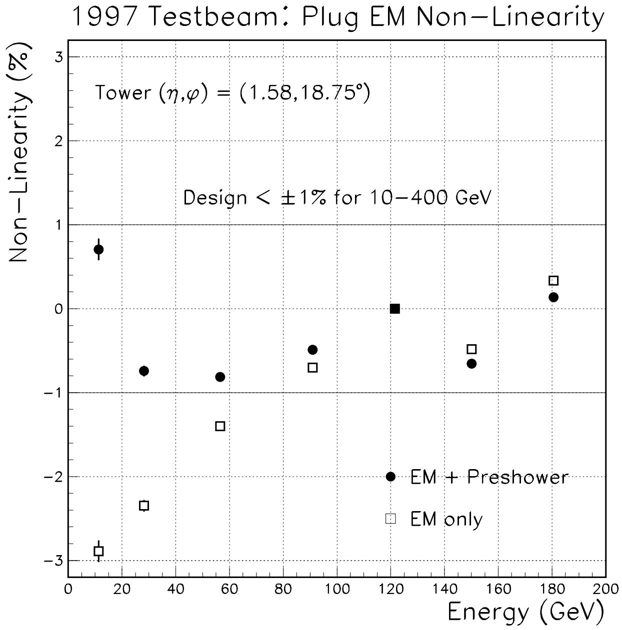

Figure 52: Non-linearity factors as a function of the electron energy with and without the correction using the PPR.

6.3 Calorimeter Performance

The calorimeter calibration by the test beam has been carried out for both of the cases with and without adding the PPR to the PEM responses [25]. The effect due to absence of the PPR readout to the calorimeter resolution was found to be very mild. The stochastic term changes from 15.2% to 15.9% at the reference tower. On the other hand, the linearity of the calorimeter is more sensitive to the PPR readout. The linearity of the calorimeter is influenced by the variation in longitudinal responses and by the material in front of the calorimeter. The requirement of the non-linearity is

$$\left(\left\langle \frac{E}{p} \right\rangle - 1\right) \times 100 < 1\%.$$

The non-linearity for low energy electrons can be reduced by adding the response of the PPR to the EM energy with a weight factor to compensate a non-detected energy. Figure 52 shows the observed and corrected non-linearity with the PPR energy as a function of the incident electron energies. The non-linearity is significantly reduced by using the PPR energy. It is possible, however, to get the calorimeter response linear by applying a correction as a function of the measured momentum which has been obtained by the test beam or will be obtained by an *insitu* calibration, rather than attempting the correction at the detector level.

Element		Quan.	Unit	Cost/Unit M&S($)/Unit	Cost/Unit Labor($)/Unit	Sub-total K$	Cont.	Total K$
Plug preshower								87.7
PPR pizza-pans								Completed.
Optical cables								Completed.
Photon readout						13.0	20%	15.6
1	MAPMT	72	each					Completed.
2	Signal cables	72	each	150.0		10.8		
3	CAEN HV crate	1	each					Completed.
4	CAEN HV distribution card (24ch)	3	each					Completed.
5	HV cables	72	each	30.0		2.2		
PPR Preradiator								Completed.
Installation						2.2	20%	2.6
1	MAPMT	60	m-hrs		20.6	1.2		
2	Signal cables	40	m-hrs		20.6	0.8		
3	CAEN	40	m-hrs					No new cost.
4	HV cables	10	m-hrs		20.6	0.2		
Readout Electronics						55.6	25%	69.5
1	SMQIE chip (2ch)	480	each					Completed.
2	SQUID card (4ch)	240	each	120.0		28.8		
3	SMD board (48ch)	24	each	770.0		18.5		
4	Crate, power supply, controller	6	each			Completed.	(A part of PES)	
5	SMD-SMXR cables	24	each	100.0		2.4		
6	AUX cards	24	each	125.0		3.0		
7	PMT-AUX cables	72	each	40.0		2.9		
Testbeam module - PPR								Completed.

Table 8: Cost elements for the PPR.

7 Calibration

The responses of 16 channels in an MAPMT will be determined using muons, which are used to set the thresholds for detecting photon conversions and for separating electrons from the background. The gain stability of the MAPMT's will be checked by using ^{137}Cs source signals. The response to electrons will be calibrated using those from W/Z decays. It is possible to estimate the amount of the material in front of the PPR using reconstructed $\pi^0/\eta \to \gamma\gamma$ and $\rho^+ \to \pi^+\pi^0$ in the shower maximum detector, for which we will need a special lower-p_T photon trigger, as we used for the CPR in Run I.

8 Cost Estimation and Schedule

A significant fraction of cost elements has been covered by now. The MAPMT's have been purchased already. Also, there exist unused channels in, for example, the HV system for the plug shower max detector due to the system modularity, which is able to accommodate the PPR. The biggest cost is for ADC's, and the total is expected to be $\simeq$ \$87.7k. The cost elements are listed in Table 8.

In order to avoid cabling in the collision hall, at least the signal cables and HV cables must be in place prior to the detector roll-in. The PPR layer is implemented with permanent sources, thus the wire source calibration will be possible after the detector roll-in. Optical cable connection is now in progress assuming the PPR installation. They will be secured with light tightening in the course of the work. Unless we provide the PPR readout or reconnect optical cables with breaking the light tight systems, the detector

Place all the PO's	in fall 1999
Installation of tubes and ADC's	by spring 1999
Wire sourcing	by summer 1999
Complete	by Sep, 1999

Table 9: A PPR installation schedule.

information from the first layer of the PEM will be lost.

We expect no difficulty in the PPR installation because it can be merged into setting up the baseline detector smoothly. A general schedule we want to follow is given in Table 9.

9 Summary

The identification of photons and electrons in the plug region will be significantly improved with the CDF II detector because of the coverage extension of the silicon tracking system and the calorimeter upgrade. The PPR will further extend the physics capability of the CDF II. The main purposes of the preshower detector are the statistical separation of the prompt photons in a wide energy range, and the event-by-event rejection and/or the statistical separation of the charged hadron backgrounds in the electron identification.

The plug region is very important for the QCD photon physics to explore extended kinematical regions. Also, the plug photons provide significant acceptance gains, for example, for $W\gamma$ events. From the test beam data analysis, the PPR is expected to have enough capability for the statistical separation of photons.

Similarly, the plug electrons contribute to expanding the kinematical regions accessible by the CDF II and to statistics gains in various physics processes. However, the S/N in the plug region with respect to the central region is $0.3 \sim 0.8$ depending on the physics process. It is worse than the central even for the high p_T electrons, for example, in $t\bar{t}$ events. Given that the expected reduction factor of the PPR against the charged hadron backgrounds is $\simeq 2$, the PPR installation and inclusion of the PPR information in the electron selection criteria are necessary to improve the plug electron quality as good as that in the central region.

Total cost for the PPR installation is $\simeq$ \$87.7k which is dominated by the readout electronics.

Since the installation of the PPR is quite straightforward, no major problem is expected in the schedule. The electrical cables (signal cables and HV cables) at least must be installed prior to the detector roll-in. The optical cables will be connected to channels assuming the PPR installation. The information from the first layer of the PEM will be lost unless the PPR readout is present.

References

[1] CDF Collaboration, CDF II Technical Design Report, FERMILAB-Pub-96/390-E (1996) 9-1.

[2] Jim Strait, CDF note 2097; M. Albrow *et al.*, CDF note 2453.

[3] T. Ino and S. Kuhlmann, CDF note 3614.

[4] F. Abe *el al.*, Phys. Rev. D 48 (1993) 2998.

[5] R. Harris, R. Blair, and S. Kuhlmann, CDF note 2318; S. Kuhlmann and A. Maghakian, CDF note 2478.

[6] R. Harris, CDF note 1472.

[7] F. Abe *el al.*, Phys. Rev. Lett. 73 (1994) 2662.

[8] F. Abe *el al.*, Phys. Rev. Lett. 71 (1993) 679.

[9] F. Abe *el al.*, Phys. Rev. D 57 (1998) 1359.

[10] F. Abe *el al.*, Phys. Rev. Lett. 77 (1997) 5005.

[11] R. S. Fletcher, F. Halzen, and E. Zas, Phys. Rev. Lett. B221, 403 (1989); M. Stratmann and W. Vogelsang, Phys. Rev. D 52 (1995) 1535.

[12] E. L. Berger and L. E. Gordon, Phys. Rev. D 54 (1996) 2279.

[13] R. Blair, J. Huston and T. Takano, CDF note 3624.

[14] J. Olsen, CDF note 4520 and 4557.

[15] F. Abe *et al.*, CDF note 3979, submitted to Phys. Rev. Lett.

[16] A. Scott, Y. Bonushkin, J. Hauser and D. Saltzberg, CDF note 4539.

[17] Future ElectroWeak Physics at the Fermilab Tevatron, Report of the TeV_2000 Study Group, Editors D. Amidei and R. Brock, FERMILAB-Pub-96/082.

[18] G. Kane, C.P. Yaun and G. Ladinsky, Phys. Rev. D 45 (1992) 124.

[19] D. Winn and D. Amidei, CDF note 4464.

[20] M. C. Smith and S. Willenbrock, Phys. Rev. D 54 (1996) 6696; T. Stelzer, Z. Sullivan and S. Willenbrock, *ibid.* 56 (1997) 5919; T. Tait and C.P. Yaun, hep-ph/9710372.

[21] L. Demortier, T. Kikuchi and S.H. Kim, CDF note 4542.

[22] Y. Seiya *et al.*, "Test Beam Results of a Preshower Detector for the CDF Plug Upgrade", in preparation to be submitted to Nucl. Instr. and Meth. in Phys. Res. A.

[23] S. Kuhlmann, CDF note 1248.

[24] C. Campagnari, D. Kestenbaum and A. Yagil, CDF note 2960.

[25] Y. Seiya *et al.*, "Test Beam Calibration of the CDF Plug Upgrade Calorimeter", in preparation to be submitted to Nucl. Instr. and Meth. in Phys. Res. A.